

Influences of ENSO on Stratospheric Variability, and the Descent of Stratospheric Perturbations into the Lower Troposphere

YING LI

AU1

Program in Atmospheric and Oceanic Sciences, Princeton University, Princeton, New Jersey

NGAR-CHEUNG LAU

NOAA/Geophysical Fluid Dynamics Laboratory, Princeton, New Jersey

(Manuscript received 2 August 2012, in final form 20 December 2012)

ABSTRACT

The linkage between El Niño–Southern Oscillation (ENSO) and North Atlantic Oscillation (NAO) through the stratospheric pathway is examined using a global coupled climate model [GFDL Climate Model version 3 (CM3)], with increased vertical resolution and extent in the stratosphere as compared to an earlier model [GFDL Climate Model version 2 (CM2)]. It is demonstrated that the relationship between ENSO and NAO is stronger in CM3 than in CM2.

It is found that ENSO plays an important role in modulating the frequency of occurrence of the stratospheric polar vortex anomalies through enhancement/attenuation the amplitudes of zonal wavenumbers 1 and 2, especially in late winter. A higher frequency of weak (strong) stratospheric vortex events is simulated in CM3 during El Niño (La Niña) episodes.

The weak vortex events during El Niño winters are preceded by enhancement of the zonal wave-1 pattern, and weakening of zonal wave-2 pattern. These modified tropospheric planetary waves propagate upward and then weaken the stratospheric polar vortex through eddy–mean flow interaction. The zonal-mean geopotential response in the stratosphere propagates downward and weakens the polar vortex throughout the troposphere.

The effects of planetary wave refraction in the upper troposphere on the zonally averaged circulation cells in the tropospheric meridional plane, and the linkage between the lower branches of these cells and the near-surface wind patterns, play an important role in the flow pattern over the region corresponding to the southern lobe of the NAO. Specifically, a negative annular mode and NAO response is discernible in weak stratospheric vortex events during El Niño. Conversely, the positive annular mode and NAO is evident in strong vortex events during La Niña.

1. Introduction

El Niño–Southern Oscillation (ENSO) and the North Atlantic Oscillation (NAO) are two of the most prominent modes of climate variability over the Northern Hemisphere (NH) (e.g., Bjerknes 1969; Horel and Wallace 1981; Branston and Livezey 1987; Hurrell 1995; Hurrell and van Loon 1997; Trenberth et al. 1998).

Current affiliation: Department of Atmospheric Science, Colorado State University, Fort Collins, Colorado.

Corresponding author address: Ying Li, Department of Atmospheric Science, Colorado State University, 3915 W. Laporte Ave., Fort Collins, CO 80521.
E-mail: yingli@atmos.colostate.edu

Recently, the late winter teleconnection between ENSO and NAO through the tropospheric pathway related to transient eddies has been investigated by Li and Lau (2012a,b). By analyzing the output from a 2000-yr-long simulation of the Geophysical Fluid Dynamics Laboratory Climate Model version 2.1 (GFDL CM2.1), performing parallel diagnosis of reanalysis datasets, and experimentation with an atmospheric component of CM2.1 (i.e., AM2.1), they have explicitly shown that the eddy-induced negative height tendency extends eastward to the North Atlantic (NA) region during warm ENSO winters. They further presented evidence on the downstream development of the wave packets to the Atlantic storm track region in the course of the persistent episodes during El Niño. The subsequent barotropic forcing of the synoptic-scale eddies embedded in the wave packets over

DOI: 10.1175/JCLI-D-12-00581.1

© 2013 American Meteorological Society

the NA is conducive to the formation of a slowly varying flow pattern that resembles the negative phase of the NAO. Conversely, alteration of the development path of the transient disturbances during La Niña leads to positive phase of the NAO.

In addition to the above pathway in the troposphere, ENSO has also been found to influence the extratropical circulation in the stratosphere in both observational and model studies. Early observational works (e.g., van Loon and Labitzke 1987; Hamilton 1993) have provided evidence for El Niño events to produce a weakened stratospheric polar vortex through an intensification of the Aleutian high in lower stratosphere. On the other hand, the polar vortex during La Niña events is anomalously strong. However, the connection between ENSO and the zonal-mean circulation of the extratropical stratosphere is somewhat inconclusive in these observational studies, due to the difficulty of isolating ENSO effects from other sources of natural variability, such as the quasi-biennial oscillation (QBO; e.g., Hamilton 1993; Baldwin and O'Sullivan 1995).

Recent studies based on reanalysis data have found statistically significant warming in the polar stratosphere during El Niño winters (e.g., García-Herrera et al. 2006; Camp and Tung 2007; Garfinkel and Hartmann 2008b). Using different GCMs for the middle atmosphere, the distinct emergence of a stratospheric response to El Niño events and enhanced tropospheric driving of stationary wave 1 have been demonstrated (Sassi et al. 2004; Taguchi and Hartmann 2006; Manzini et al. 2006; Ineson and Scaife 2009). The effects of La Niña on the stratospheric polar vortex are less certain. A stronger than normal polar vortex has been reported during La Niña winters (Limpasuvan et al. 2005; Manzini et al. 2006; García-Herrera et al. 2006), although the signal is weak.

The anomalous stratospheric polar vortex can in turn affect the late winter climate in the North Atlantic–European (NAE) region through downward propagation of the pertinent atmospheric signals (e.g., Baldwin and Dunkerton 2001; Sassi et al. 2004; García-Herrera et al. 2006; Manzini et al. 2006). Different dynamical mechanisms have been proposed to explain the effects of the stratospheric changes on the troposphere. One is the downward control mechanism associated with the meridional circulation (e.g., Haynes et al. 1991; Thompson et al. 2006) and the equivalent inversion of the stratospheric potential vorticity (Hartley et al. 1998; Black 2002; Ambaum and Hoskins 2002). A second mechanism is the downward planetary wave reflection in the stratosphere (Perlwitz and Harnik 2003, 2004). A third mechanism is related to the impact of the stratospheric circulation on the index of refraction of vertically propagating waves (e.g., Chen and Robinson 1992;

Hartmann et al. 2000; Shindell et al. 2001). Additionally, the modulation of tropospheric synoptic eddies can feed back on the downward influence from the lower stratosphere (Kushner and Polvani 2004; Song and Robinson 2004; Chen and Held 2007).

Given the evidence on the influence of ENSO on the stratosphere polar vortex, and the possible downward influence of the polar vortex on the phase of NAO, it is anticipated that ENSO can remotely affect the NAE climate through stratospheric dynamics. The possible link between ENSO and the NAE climate via the stratospheric pathway has been noted recently (Brönnimann et al. 2004; Bell et al. 2009; Cagnazzo and Manzini 2009; Ineson and Scaife 2009). However, most of those previous studies focus on the linkage between the warm phase of ENSO and the weakening of the stratospheric polar vortex, and the subsequent negative northern annular mode (NAM) signature near the surface. In this work, the two opposing phases of ENSO and both the strong and weak stratospheric vortex events are considered. We shall also investigate the roles of vertical and meridional planetary wave propagation in the upper troposphere in linking ENSO to NAO.

As indicated in Li and Lau (2012a), due to the low vertical resolution of the stratospheric region in CM2.1, the ENSO effect on the simulated extratropical stratosphere is very weak. The ENSO–NAO relationship identified in the CM2.1 simulation is primarily due to the tropospheric pathway. In this study, we use an 800-yr integration of another general circulation model with a more realistic upper atmosphere (GFDL CM3; see Donner et al. 2011), and compare the ENSO–NAO link as simulated in this model with that in CM2.1. Such comparison provides insights into the impact of stratospheric processes on the ENSO–NAO relationship. The long duration of the CM3 integration allows for adequate sampling of the pertinent features associated with ENSO and the variability in the stratospheric polar vortex, and also provides for an evaluation of the statistical relationship between ENSO and circulation changes in the stratosphere with a high degree of confidence. Such analysis is not feasible with the limited observational record.

The remainder of this paper is organized as follows. The basic datasets and analysis tools are described in section 2. Section 3 documents the seasonality of ENSO and the ENSO–NAO relationship in observations and two coupled model simulations. The characteristics of the stratospheric mean state, variability, and stationary waves are also shown in this section. In section 4, the procedure for the selection of the stratospheric strong/weak vortex events, as well as the relationships between the frequency of occurrence of strong/weak vortex

events and ENSO, are presented. The fluctuations of the planetary waves during ENSO and anomalous vortex events are examined in section 5. The wave propagation in terms of Eliassen–Palm (EP) flux, and its relationship with the meridional circulation, are analyzed in section 6. The zonal-mean zonal wind and surface pressure responses are shown in section 7. A summary and discussion are given in section 8.

2. Description of model experiment, observational datasets, and diagnostic tools

a. Model

The numerical model used in this study is the new Geophysical Fluid Dynamics Laboratory global coupled climate model CM3. The horizontal resolution of the atmospheric component of CM3 (i.e., AM3) is 2° latitude \times 2.5° longitude. The dynamical core of AM3 uses a new finite-volume core formulated on a cubed-sphere grid (Putman and Lin 2007), instead of the original latitude–longitude grid used in AM2 (Lin 2004). This new method greatly improves the computational efficiency and simulation quality in the polar region. The number of vertical layers is increased to 48 from 24 in AM2, with the model top at 0.01 hPa (Donner et al. 2011). Only four layers are above 100 hPa in AM2, whereas there are 25 layers above 100 hPa in AM3. The increased vertical resolution and extent in the model stratosphere in AM3 allow for a more detailed representation of the stratospheric chemical and dynamical processes. The dynamical core, physical parameterization, and basic simulation characteristics of the AM3 are described by Donner et al. (2011). As in AM2, orographic gravity waves are parameterized using Stern and Pierrehumbert (1988). This wave drag is included up to the 30-hPa level in AM3. The ocean component of CM3 uses the Modular Ocean Model version 4p1 (MOM4p1) code (Griffies 2009), whereas the ocean component of CM2.1 is based on the MOM4.0 code (Griffies et al. 2004). The physical parameterizations and grid resolution of the CM3 ocean component are the same as that used in CM2.1, as detailed in Griffies et al. (2005) and Gnanadesikan et al. (2006). As in Li and Lau (2012a), we choose to focus on the preindustrial (1860) control simulation of CM3. Using such control integrations allows us to eliminate the influence of externally forced climate variability on the stratosphere and troposphere, such as that due to volcanoes, aerosols, or greenhouse gases. Our model analysis is focused on the output of this 800-yr control run.

It should be noted that the vertical resolution in CM3 is still not sufficiently fine for simulating the quasi-biennial oscillation (Giorgetta et al. 2006). Thus, the possible

influence of QBO on the interannual variability of the northern winter stratospheric flow (Holton and Tan 1980, 1982) is not considered in the present study.

b. Observational datasets

The observed data used in this study are mostly based on monthly and daily mean fields (September 1957 to August 2002) from the 40-yr European Centre for Medium-Range Weather Forecasts (ECMWF) Re-Analysis (ERA-40; see Uppala et al. 2005). This dataset has a horizontal resolution of $2.5^\circ \times 2.5^\circ$ and extends from 1000 to 1 hPa with 23 vertical pressure levels. The only exception is in sections 3a and 3b, in which the National Centers for Environmental Prediction (NCEP)–National Center for Atmospheric Research (NCAR) reanalysis dataset for the 1949–2010 period is used so as to be consistent with the results of Li and Lau (2012a). Anomalies are computed by subtracting the annual cycle calculated for the 1949–2010 period. Analyses based on ERA-40 yield similar results.

Niño-3 index (SST anomalies averaged over 5°S – 5°N , 150° – 90°W), based on the National Oceanic and Atmospheric Administration (NOAA) Extended Reconstructed SST version 3 dataset (ERSST V3; see Smith et al. 2008; Xue et al. 2003), is used as an indicator of ENSO variability.

c. Diagnostic tool

In the quasigeostrophic (QG) approximation, the EP flux in spherical and log-pressure coordinates (Edmon et al. 1980; Vallis 2006) can be written as

$$F_\phi = -\rho_0 a \cos\phi [v^*u^*], \quad (1)$$

$$F_z = f\rho_0 a \cos\phi \frac{[v^*\theta^*]}{[\theta]_z}. \quad (2)$$

Here the bracket (asterisk) denotes zonal means (deviation from the zonal mean). The vertical coordinate is $z = -H \ln(p/1000)$, where H is standard constant scale height (7 km). Also, ρ_0 is air density, which varies with height as $\rho_s \exp(-z/H)$, where ρ_s is a constant; a is the radius of Earth, ϕ is latitude, $f = 2\Omega \sin\phi$ is the Coriolis parameter, u and v are the zonal and meridional velocity components; finally, θ denotes potential temperature, and its partial derivative with respect to z is written as θ_z .

The EP flux is related to the acceleration of the zonal-mean zonal flow as

$$D_F \equiv \frac{1}{\rho_0 a \cos\phi} \mathbf{V} \cdot \mathbf{F}, \quad (3)$$

with the flux divergence given by

$$\nabla \cdot \mathbf{F} = \frac{1}{a \cos \phi} \frac{\partial}{\partial \phi} (F_\phi \cos \phi) + \frac{\partial}{\partial z} (F_z). \quad (4)$$

By expanding the daily u , v , and θ fields into their Fourier harmonics, the EP flux and its divergence for zonal wave 1 and 2 are calculated.

The zonal-mean meridional circulation, which is composed of $[v]$ and $[w]$, can be described by a mass streamfunction, which is defined by calculating the northward mass flux above a particular level p , and given by

$$\Psi_M = \frac{2\pi a \cos \phi}{g} \int_0^p [v] dp. \quad (5)$$

For calculations involving the EP flux, the daily u , v , and θ are used to compute the daily fields of EP flux. Monthly mean EP flux is then computed from the monthly average of the daily EP flux. In this way, contributions of both stationary and transient waves are included. The climatological annual cycle is computed by long-term averaging of each calendar month, and the annual cycle is then removed from the monthly EP flux to produce the monthly EP flux anomalies. Analogously, the monthly anomalies for other fields are defined by removing the corresponding climatological annual cycle.

According to the convention described in Dunkerton et al. (1981), the respective values of F_ϕ and F_z are multiplied by factors proportional to the distances occupied on the diagram by one radian of latitude, and one meter of $-H \ln(p/1000)$, so that \mathbf{F} determines the directions and relative magnitudes of the arrow uniquely in the diagram. In addition, the EP flux vectors are scaled by the inverse of the air density at the given level so that some indication of wave propagation in the stratosphere is possible.

3. Simulation of ENSO, NAO, and stratospheric variability

a. Phase locking of ENSO to the seasonal cycle

As in Li and Lau (2012a), a warm (cold) ENSO event is identified when the December–February (DJF)-mean Niño-3 index is more than one standard deviation (σ) above (below) the time mean. The selected ENSO events in both observations and the CM2.1 simulation are the same as in Li and Lau (2012a). Figure 1 shows the composite month-to-month evolution of the Niño-3 SST anomalies during El Niño and La Niña events for the observations and two coupled model simulations. The observed El Niño and La Niña events exhibit a tendency to reach peak amplitudes toward the end of year(0) (see black curves in Fig. 1). However, it is evident that the peak Niño-3 SST anomalies in both models occur in late

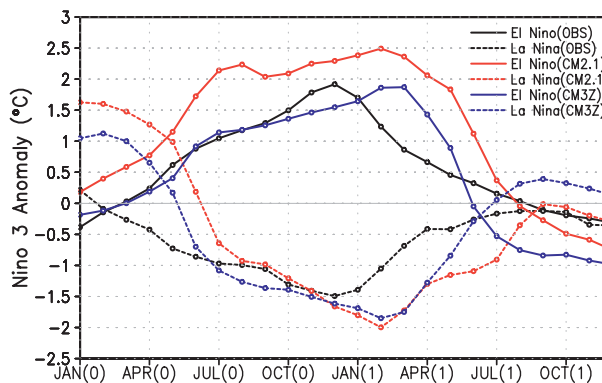


FIG. 1. Composite monthly evolution of the Niño-3 SST anomalies for El Niño (black solid curve) and La Niña (black dashed curve) events in observations, El Niño (red solid curve) and La Niña (red dashed curve) events in the CM2.1 simulation, and El Niño (blue solid curve) and La Niña (blue dashed curve) events in the CM3 simulation. The abscissa represents a 24-month period from January of year(0) to December of year(1). A specific month in this period is identified by a label consisting of the first three letters of that month, followed by the year indicator (0 or 1) in parentheses. The year of initiation of the selected ENSO event is designated as year(0); the following year is referred as year(1). For instance, Dec(0) refers to the month of December in year(0).

winter [i.e., near Feb(1)]. It should also be noted that the typical amplitude of the El Niño events in CM3 is noticeably smaller than that in CM2.1, and is in better agreement with the observations. The faster than normal decay for both El Niño and La Niña events in the CM3 simulation could result from the model bias toward a quasi-biennial ENSO period (A. T. Wittenberg xxxx, [AU2](#) personal communication).

b. ENSO–NAO relationship

To illustrate the seasonality of the anomalous surface pressure pattern over the NA sector associated with ENSO, the regression coefficients of the sea level pressure (SLP) field versus the Niño-3 index are computed, and their dependence on calendar month and latitude is shown in Fig. 2. Results for the averages over the longitudes between 70° and 20°W are presented. During the Jan(1)–Apr(1) period, the observed pressure pattern (Fig. 2a) is characterized by a low pressure anomaly to the south, and a high pressure anomaly to the north, corresponding to the negative phase of NAO. This SLP configuration is captured in both of the model experiments (Figs. 2b,c), except that the simulated positive anomaly peaks two months after the negative anomaly attains maximum amplitude. As noted in Li and Lau (2012a), it is plausible that the difference in the occurrence of NAO signals between observations and model simulation might be related to the 1-month delay of the tropical Pacific SST forcing in the simulation relative to

F1

AU2

F2

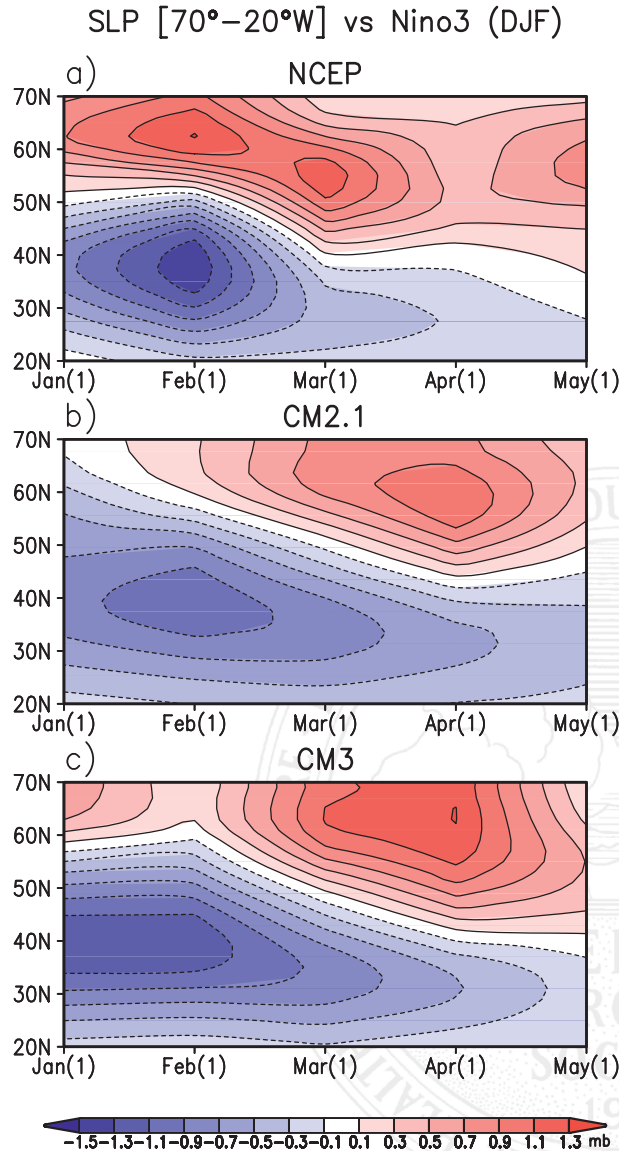


FIG. 2. Time-latitude variations of the regression coefficients of SLP anomalies vs standardized DJF-mean Niño-3 index, as computed using the (a) NCEP-NCAR reanalysis, (b) CM2.1 simulation and (c) CM3 simulation. Contour interval is 0.2 hPa. Results are shown for averages over the 70°–20°W sector.

the observations, as illustrated in Fig. 1. The amplitude of dipolar anomaly in the CM3 simulation is about 20% larger than that in the CM2.1 simulation. The relatively stronger amplitude of SLP anomaly in the CM3 simulation is in better agreement with the observations.

In addition, the observed ENSO-related responses of the negative SLP anomaly centers over NA are noted to be shifted northeastward as compared to the classical NAO pattern (e.g., Brönnimann 2007). Such northeastward shift is evident in the CM2.1 simulation (see Fig. 7 in Li and Lau 2012a) but not evident in the CM3

simulation (not shown), with the negative center closely corresponding to the southern lobe of NAO. The linear correlation between Niño-3 and NAO indices (the normalized temporal coefficients of the leading EOF of the SLP field over the NA region in the January–April-mean winter season) is also strengthened in the CM3 simulation (–0.30 in the CM3 simulation versus –0.23 in the CM2.1 simulation).

The above differences in the NAO-like signal between these two models could be due to the role of the stratosphere, as facilitated by the enhanced vertical resolution in the CM3 model. This motivates us to verify whether ENSO teleconnection through the stratospheric pathway is a possible factor contributing to the stronger NAO-like SLP response to ENSO in the NA region.

c. Characteristics of troposphere and stratosphere stationary waves

The observed NH wintertime climatological [November–March (NDJFM) mean] stationary wave field (the time-averaged geopotential height with the zonal mean removed, $\bar{Z}^* = \bar{Z} - [\bar{Z}]$), along with its first two zonal harmonic wave components, are shown in the top half of Fig. 3. The stationary wave in the upper troposphere (300 hPa) is characterized by troughs and ridges over the western and eastern oceans, respectively (Fig. 3d). The stratospheric stationary wave pattern at 10 hPa (Fig. 3a) is dominated by a zonal wavenumber-1 dipolar structure (Fig. 3b), with relatively minor contribution from the wavenumber-2 component (Fig. 3c). This wave-1 pattern features a stationary cyclone over the Eurasian continent and an anticyclone over the Aleutian Islands, thus indicating that the center of the climatological Arctic vortex is displaced toward the Eurasian continent.

The phases of both the stationary waves 1 and 2 at 10 hPa are shifted westward with respect to those at 300 hPa. This pronounced westward tilt of the geopotential height perturbations with height is indicative of vertically propagating waves from the mid- and high-latitude troposphere. The dominance of planetary-scale waves in the stratosphere is primarily due to the filtering effect of the basic state on higher-wavenumber waves as they make their entry to the stratosphere (Charney and Drazin 1961; Andrews et al. 1987).

The simulated wintertime climatological stationary wave (bottom half of Fig. 3) is very similar to the observations. The local extrema at both 300 hPa and 10 hPa are captured by the model simulation. The simulated zonal wave-1 and -2 structures are nearly identical to the corresponding observed patterns. The primary difference between the observed and simulated stationary

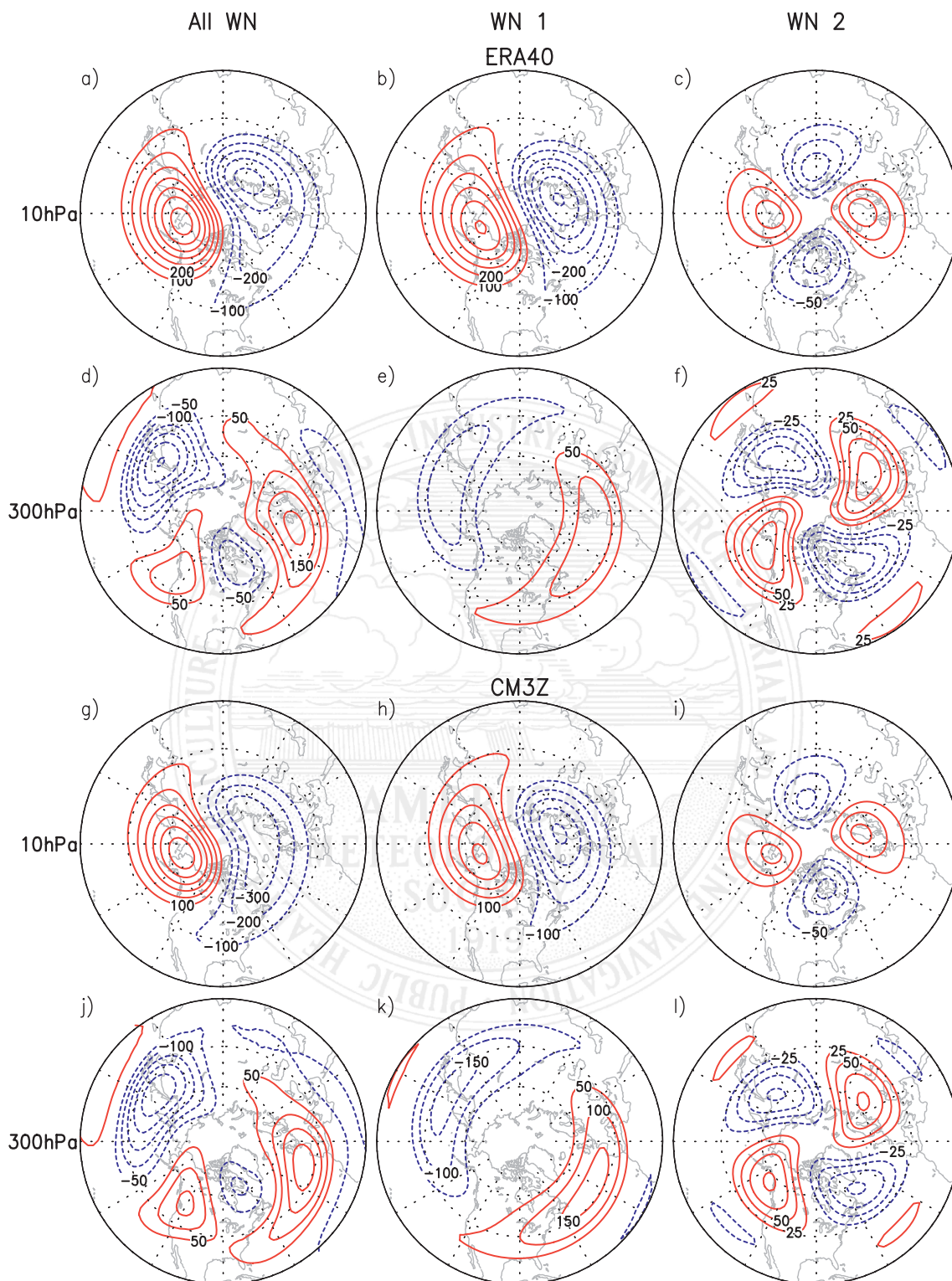


FIG. 3. Climatological (left) all-wavenumber, (middle) zonal wavenumber-1, and (right) wavenumber-2 patterns of geopotential height fields at 10 hPa (first and third rows) and 300 hPa (second and fourth rows). Results are based on NDJFM-mean of (top half) ERA-40 reanalysis and (bottom half) CM3 simulation. In all plots, positive and negative contours are colored red and blue, respectively, and the zero contour is omitted. The contour interval in the zonal wavenumber-1 pattern is the same as that in the all-wavenumber pattern, that is, 100 m at 10 hPa for plots in (a),(b),(g), and (h) and 50 m at 300 hPa for plots in (d),(e),(j), and (k). The contour interval in the zonal wavenumber-2 chart is half of that in the all-wavenumber chart, that is, 50 m at 10 hPa for plots in (c) and (i) and 25 m at 300 hPa for plots in (f) and (l).

wave structures is found in the amplitude of wave-1 component. For instance, the amplitude in the simulation is noticeably larger than that in observations at 300 hPa (cf. Figs. 3e and 3k), whereas the simulated amplitude at 10 hPa is smaller than the observed counterpart (cf. Figs. 3b and 3h). This difference indicates the reduced amplitude growth with height of the wave-1 component in the model simulation, which appears to be attributable to the insufficient upward propagation of the planetary waves. Since the vertical component of the EP flux is proportional to the poleward eddy heat flux [see Eq. (2)], this underestimation of upward EP fluxes is also a contributing factor to the cold bias in the Northern Hemisphere winter stratosphere (Donner et al. 2011).

It should be noted that although the climatological stationary wave at 300 hPa is realistically simulated in CM2.1, the simulated amplitude of both stationary waves 1 and 2 at 10 hPa are reduced by a factor of 2 (not shown). The much damped waves at 10 hPa are due to the existence of sponge layer near the model top of AM2. As noted in Fletcher and Kushner (2011), the simulated response of the extratropical annular mode to climate forcing is highly dependent on the accurate simulation of the phase and amplitude of the climatological stationary wave structure. The generally realistic background stationary wave in the CM3 simulation lends confidence in interpreting the linear interference between the anomalous wave response and the climatological stationary waves as discussed later in section 5.

4. Relationships between ENSO and stratospheric vortex anomalies, and their seasonal dependence

a. Identification of anomalous stratospheric polar vortex months

As a measure of the intensity of the stratospheric vortex, a monthly mean (November to March) polar vortex strength index is obtained by computing the areal average of the geopotential height anomaly over the polar cap region north of 70°N, and by performing a mass-weighted average over the air column between 3 and 30 hPa. The index thus obtained has been used in many recent studies (e.g., Garfinkel et al. 2010; Kolstad et al. 2010; Kolstad and Charlton-Perez 2011) and is shown to be almost identical to the NAM index based on the empirical orthogonal function analysis. The index used in our study is also more effective than zonal wind speed at 60°N for studying the stratosphere–troposphere coupling (Baldwin and Thompson 2009). A negative anomaly in our vortex strength index corresponds to anomalously low heights and a strong vortex, whereas a positive anomaly implies a weak vortex.

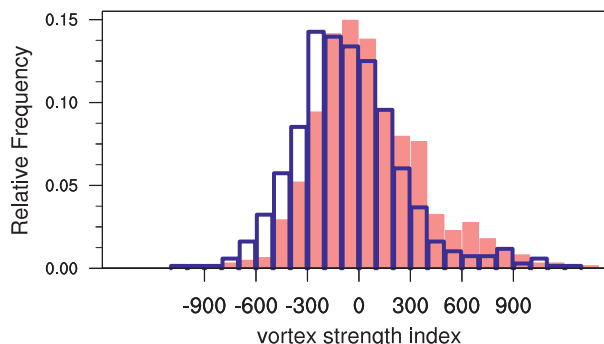


FIG. 4. Frequency distribution of the monthly (November–March) vortex strength indices for the selected El Niño winters (red filled columns) and La Niña winters (blue unfilled columns) in the CM3 simulation.

The probability distribution function of the vortex strength index has a Gaussian shape, with a slight skewness toward positive anomalies (see examples in Fig. 4). Months of weak and strong stratospheric vortex are defined as those months in which the vortex strength index is greater than the 90th percentile (+385.8 m) and less than 10th percentile (−346.5 m) for the cold season (NDJFM), respectively.

The frequency of occurrence of weak and strong vortex events in each calendar month from November through March, based on both the ERA-40 reanalysis and CM3 simulation, has been examined. The results show that most of the weak and strong vortex events occur from December to March in both observations and models. The frequency peaks in January and February for ERA-40 reanalysis. However, the model simulation shows the tendency for both the strong and weak vortex events to occur later than observed, with the highest frequency in February and March.

b. The dependence of the stratospheric vortex anomalies on the phase of ENSO

Figure 4 compares the frequency distribution of the monthly stratospheric vortex strength indices for 123 El Niño winters with the corresponding distribution for 136 La Niña winters. The ENSO events are selected by the same criteria as in section 3a, except that the NDJFM-mean Niño-3 index is used, so as to be consistent with the definition of the cold season for computing the anomalous stratospheric vortex index in section 4a. This figure illustrates that strong positive vortex indices (greater than 300 m) are more frequent in El Niño years than in La Niña years. Conversely, strong negative vortex indices (less than −300 m) are more frequent in La Niña years than in El Niño years.

A higher frequency of months with weak (strong) stratospheric vortex under El Niño (La Niña) conditions

TABLE 1. The number of weak and strong vortex months for all winters, El Niño winters, and La Niña winters based on the CM3 simulation. The El Niño and La Niña winters are defined when the NDJFM-mean Niño-3 index is more than 1σ above and below the time mean, respectively. The weak (strong) vortex month is defined when the monthly mean polar vortex strength index is greater (less) than its wintertime (NDJFM) 90th (10th) percentile. The numbers in parentheses indicate the subset of weak/strong vortex months actually used in the composite analysis. The numbers in parentheses are smaller than the total number of strong/weak vortex months due to treatment of events lasting for two or more consecutive months (see text in section 5a for details).

	Weak vortex	Strong vortex
All winters	400 (303)	400 (295)
El Niño	87 (64)	37 (27)
La Niña	47 (37)	103 (76)

is also evident from the data entries in Table 1. For example, the number of weak vortex months (87) exceeds the number of strong vortex months (37) by a factor of 2–3 in El Niño winters. Conversely, a strong vortex is 2–3 times more likely to occur than a weak vortex in La Niña winters (i.e., 103 vs 47). The probability of the occurrence of weak vortex events in El Niño winters [(87 months)/(123 yr \times 5 months) = 0.1414] is significantly larger than that in La Niña winters [(47 months)/(136 yr \times 5 months) = 0.0764], with $p < 0.0001$ based on a χ^2 test. Likewise, the probability of the occurrence of strong vortex events is also significantly different in El Niño and La Niña winters ($p < 0.0001$). These results are consistent with the previous studies on the influence of ENSO teleconnection on the wintertime Northern Hemisphere stratospheric polar vortex (e.g., Sassi et al. 2004; Manzini et al. 2006; Brönnimann 2007; Bell et al. 2009; Ineson and Scaife 2009).

5. Behavior of planetary-scale tropospheric and stratospheric waves during ENSO and anomalous polar vortex events

a. Planetary wave precursors one month before the weak/strong vortex events

As extratropical waves propagate vertically from the extratropical troposphere to the extratropical stratosphere, tropospheric anomalies typically precede the wave activity in the upper atmosphere. The tropospheric precursors of stratospheric polar vortex anomalies have been reported in recent studies (e.g., Garfinkel et al. 2010; Kolstad and Charlton-Perez 2011). In this subsection, the precursory signals leading to weak/strong vortex events are examined by computing composites of geopotential height anomalies in the month just prior to these episodes. Some ambiguity arises in those cases

when the events last for two or more consecutive months. In such instances, only the data preceding the first month of these long-lived episodes are considered in the composite analysis, following the methodology of Kolstad and Charlton-Perez (2011). The number of cases included in this procedure is indicated in parentheses in Table 1. These cases constitute a subset of total inventory of months with weak/strong polar vortices (see data entries in Table 1 without parentheses).

Figure 5 shows the longitude–height cross sections of the wave-1 (left panels) and wave-2 (right panels) components of geopotential height, as averaged from 45° to 75°N , and at 1 month prior to the weak vortex (upper panels) and strong vortex events (lower panels). To assign equal weights to individual events, the anomalies of individual events have been normalized by the amplitude of the standardized vortex strength index. Thus the composites in Fig. 5 represent anomalies corresponding to a 1σ change in the vortex strength index. In Fig. 5 (and in Figs. 6 and 8 to follow), the climatological (NDJFM mean) stationary wave fields are shown in black contours, and the anomalous wave patterns are presented using shading.

It is evident from Fig. 5 that weak vortex events are preceded by an enhancement of both planetary wave-1 and -2 patterns (Figs. 5a,b); whereas the strong vortex events are preceded by suppressed wave-1 and -2 patterns (Figs. 5c,d). These relationships are in accord with the discussion in section 2c on the effects of EP flux on the zonal mean flow. Specifically, increased propagation of planetary waves leads to stronger EP flux convergence in the high-latitude stratosphere, deceleration of the zonal mean flow, and reduction in the strength of the polar vortex. Conversely, attenuation of planetary wave propagation would have the opposite effect.

b. Planetary wave response during ENSO winters

To compare the amplitude and structure of the precursory planetary wave pattern during anomalous polar vortex winters with the wave response to ENSO winters, the selected El Niño and La Niña winters (see definition in section 4b) are used for constructing the composites in Fig. 6, which is plotted using the same format as Fig. 5. The composite values shown in Fig. 6 represent the height anomalies corresponding to a 1σ change in the Niño-3 index. The composites are averaged over the period of JF(1), when the response to ENSO is strongest. From late autumn to early winter, the wave response (not shown) is relatively very weak, especially for the wave-2 component.

In late winter of El Niño events, the wave-1 geopotential height anomalies are in phase with the climatological stationary wave 1, and thus enhance the stationary

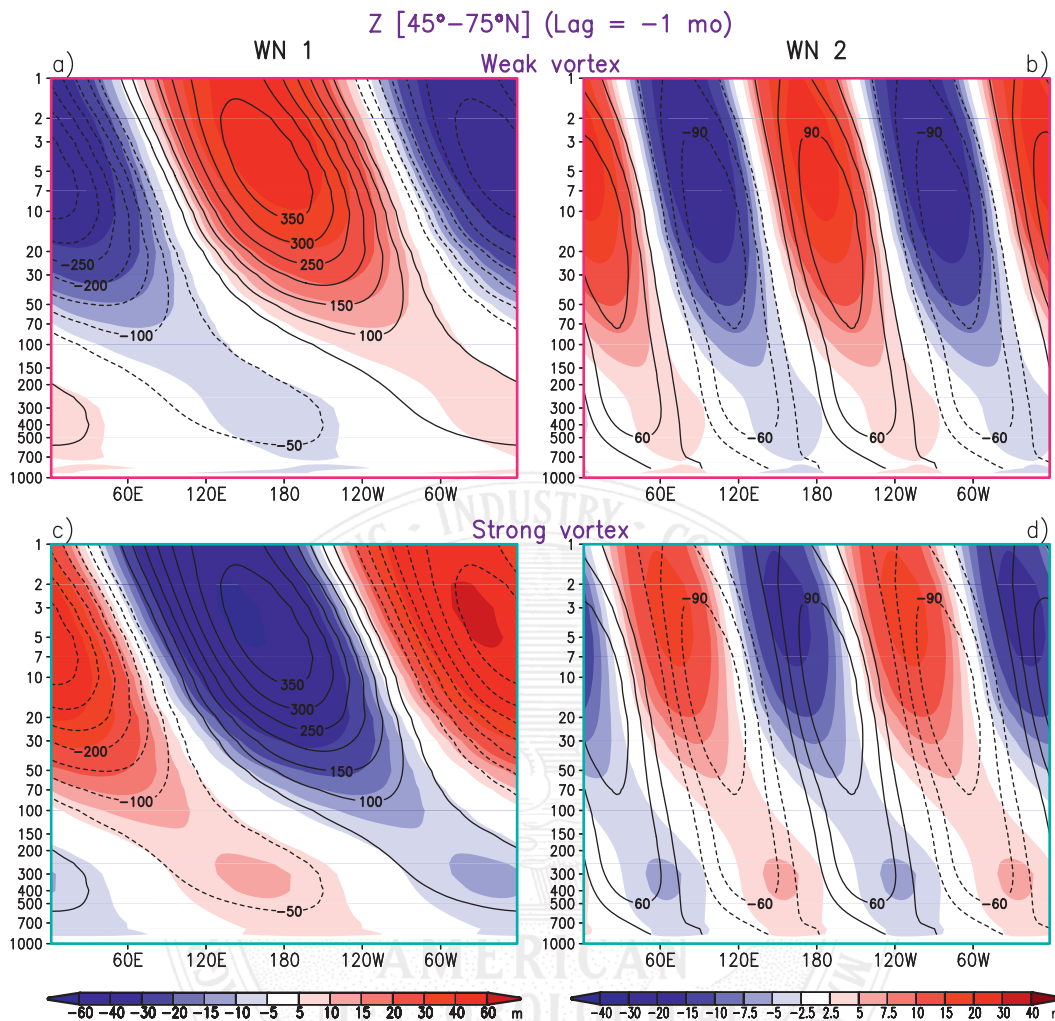


FIG. 5. Composite longitude–height cross sections of zonal (left) wavenumber-1 and (right) wavenumber-2 components of geopotential height (m) averaged between 45° and 75°N. Results are shown for climatology (NDJFM-mean; contours; interval: 30 m; dashed contours indicate negative values) and composite (top) weak and (bottom) strong vortex anomalies (shading; see scale at bottom) based on the CM3 simulation. The composites are computed during data at a lag of -1 month relative to the anomalous vortex events, and represent a 1σ change in the vortex strength index. The outer frames for those panels depicting constructive (destructive) interference between the anomalous wave pattern and the climatological stationary wave are drawn in red (blue). The results in this figure are based on the composites over the subsets of weak/strong months in all-winters (see numbers in parentheses in the first row of Table 1).

wave 1 (Fig. 6a). This feature is consistent with previous studies highlighting the amplification of climatological wave 1 during El Niño winters (Manzini et al. 2006; Garfinkel and Hartmann 2008a; Ineson and Scaife 2009), and in experiments with imposed warmings over the eastern tropical Pacific ocean (Fletcher and Kushner 2011).

In contrast, the pattern of wave-2 geopotential height anomalies (Fig. 6b) is indicative of a general weakening as well as a phase shift of the climatological stationary wave-2 pattern. This anomalous wave-2 pattern resembles the wave-2 response in experiments with

imposed warmings over both the eastern tropical Pacific and tropical Indian Ocean (see Fig. 7d in Fletcher and Kushner 2011).

Similar but opposite-signed wave-1 and -2 geopotential height anomalies are evident in the La Niña composites (Figs. 6c,d), with slight westward displacement of the anomaly centers in the La Niña composites relative to the El Niño composites. The results in Figs. 6c and 6d hence indicate weakening of wave 1, but strengthening and small phase shift of wave 2 in the late winter La Niña events.

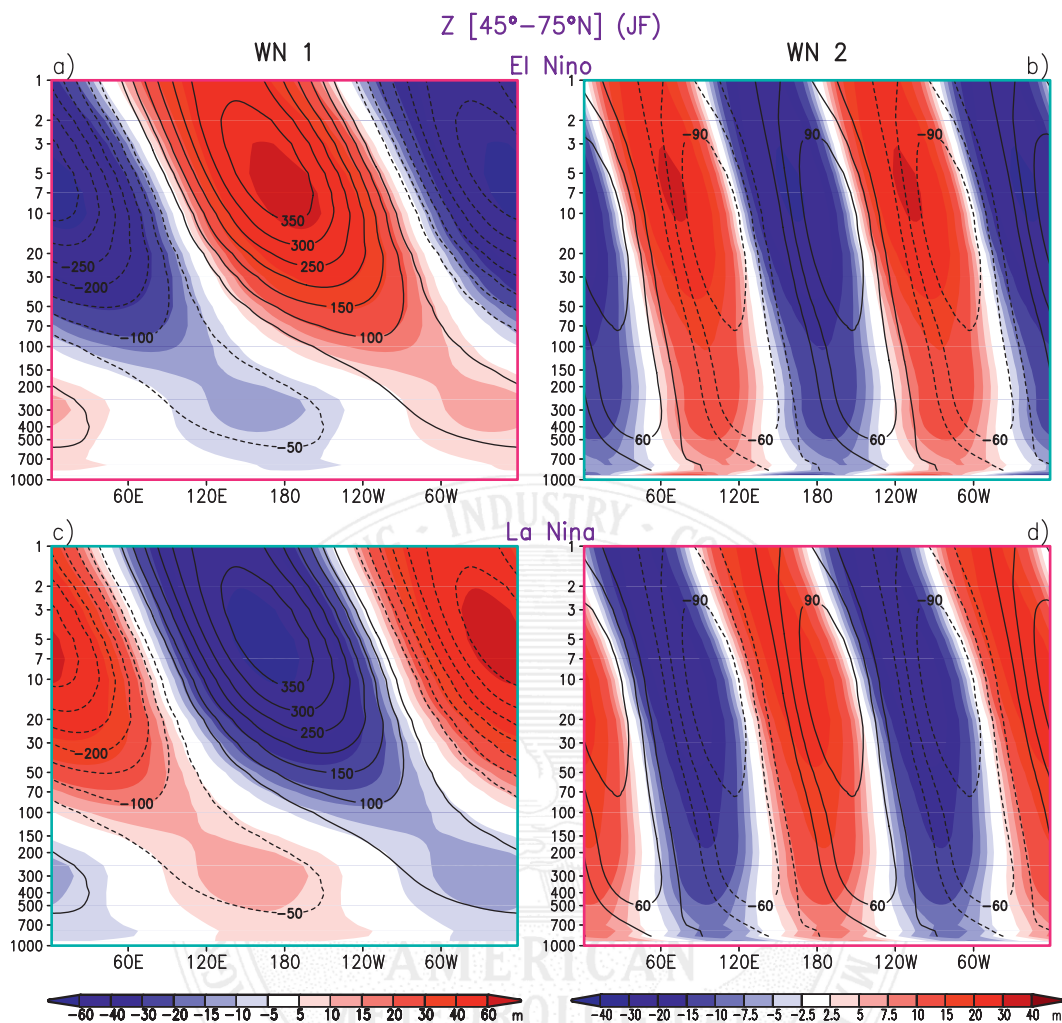


FIG. 6. As in Fig. 5, but for (top) El Niño and (bottom) La Niña events. The composites are computed for the period JF(1), and represent a 1σ change in the Niño-3 index.

c. Combinations of the ENSO responses and precursors to polar vortex anomalies

The possible interactions among the wave patterns associated with polar vortex anomalies (Fig. 5) and ENSO events (Fig. 6) are summarized by the schematic diagram in Fig. 7. Wave patterns occurring in a given type of ENSO or vortex event are indicated by a circle with a black label (see circles with notations “strong vortex,” “weak vortex,” “El Niño,” and “La Niña”). The effect of the anomaly field on the wave-1 component of the climatological stationary wave is indicated in the larger sector in each of these circles, whereas the corresponding effect on the wave-2 component is shown in the smaller sector. Enhancement and attenuation of the stationary wave amplitudes are depicted using red and blue shading, and also by the plus and minus sign, respectively. For instance, the circle with

the “weak vortex” label at the top center of Fig. 5 indicates strengthening of both wave-1 and -2 amplitudes of the stationary wave, in accord with the results in Figs. 5a and 5b.

The circles at four corners of Fig. 7 (with red and blue labels) depict the changes in amplitudes of wave-1 and -2 components of the stationary wave as a result of combinations of polar vortex and ENSO events with various polarities. For example, for the combination of El Niño and weak vortex events (see top right corner), wave 1 is significantly enhanced, since both the composite for weak vortex events (Fig. 5a) and the composite for El Niño episodes (Fig. 6a) exhibit an in-phase relationship with the wave-1 component of the climatological stationary wave. Conversely, the amplification of wave 2 in weak vortex events (Fig. 5b) opposes the weakening of this component in El Niño events (Fig. 6b), so that the combination of weak polar vortex and El Niño would

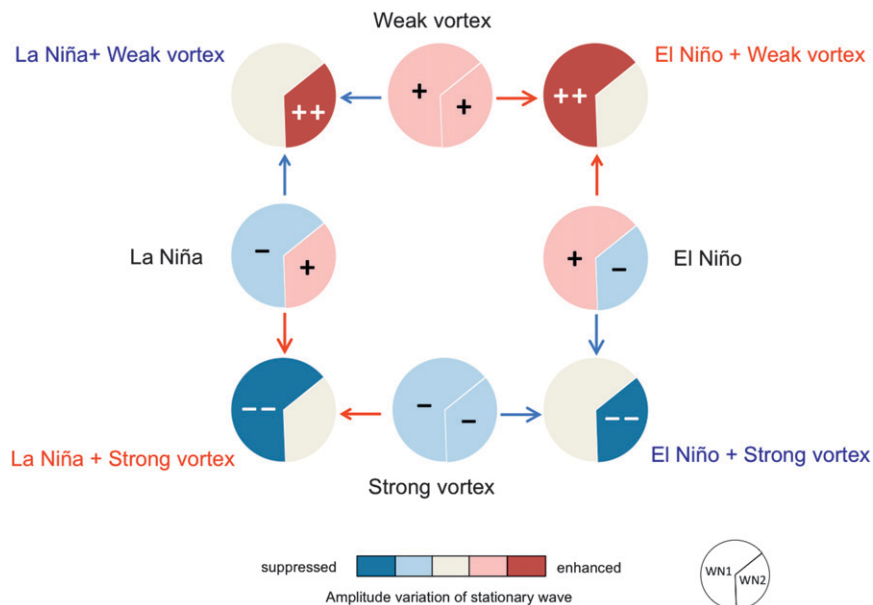


FIG. 7. Schematic diagram of the modulation of the planetary wave associated with El Niño, La Niña, strong, and weak vortex events separately (circles with black labels), and the four types of combination among these events (circles at four corners with red and blue labels). The larger sector in each of these circles illustrates the effects of the anomalies on the amplitude of the wave-1 component of the stationary wave, and the smaller sector denotes the effects on the wave-2 component (see notation at bottom right). Enhancement and attenuation of these wave components are indicated by plus and minus sign, and also by red and blue shading (see scale bar at bottom), respectively.

have minor signatures for wave 2. It can be shown by analogous arguments that the combination of La Niña and strong vortex events (see bottom left corner of Fig. 7) leads to attenuation of wave 1, and little change of wave 2. As such, the above two types of combination (i.e., El Niño/weak vortex and La Niña/strong vortex, as highlighted by red labels in Fig. 7) are characterized by a strong wave-1 structure, and will henceforth be referred to as the “wave-1 combinations.” Unlike the wave-1 combinations, the other two types of combination (i.e., El Niño/strong vortex and La Niña/weak vortex; see blue labels) do not have a large signature for wave 1 but are characterized by a noticeable wave-2 structure. Thus, they will be referred to as the “wave-2 combinations.”

We proceed to perform a composite analysis on the basis of the four types of combination as described above. The number of months used for constructing the composite for each combination is listed in parentheses in the second and third rows of Table 1). In analogy to Fig. 5, all composites are computed using the data for the month before the selected weak/strong events (also see section 5b for details of similar treatment of vortex events lasting for two or more consecutive months). Using the same format as Fig. 5, the vertical structure of the wave field is shown in Fig. 8, for the two wave-1

combinations (top two rows) and two wave-2 combinations (bottom two rows).

For the El Niño/weak vortex events, the anomalous ridge and trough in the troposphere (shading in Fig. 8a) strongly project onto the wave-1 structure (shading in Fig. 8b) and are in phase with the climatological stationary wave-1 pattern (contours in Fig. 8b). The strengthening of the planetary wave 1 is predominately due to the El Niño-related Aleutian low component of the Pacific–North American (PNA) superimposed on the climatological trough over the North Pacific (not shown). This result is consistent with findings by Garfinkel et al. (2010), who suggest that the dominant pathway through which warm ENSO modulates the vortex is the deepened Aleutian low and the increase in the planetary wave-1 driving. The wave-1 structure of extratropical height anomalies exhibit a strong westward tilt with height, and also enhance the stratospheric climatological stationary wave-1 pattern. However, the anomalous wave-2 structure is in approximate quadrature with the background wave in both the troposphere and stratosphere (Fig. 8c).

The wave field for all wavenumbers for the La Niña/strong vortex events (Fig. 8d) has a similar vertical structure as that for the El Niño/weak vortex events, but with opposite sign. In particular, strong wave-1 anomalies

F8

Z [45°–75°N] Lag = -1 mo

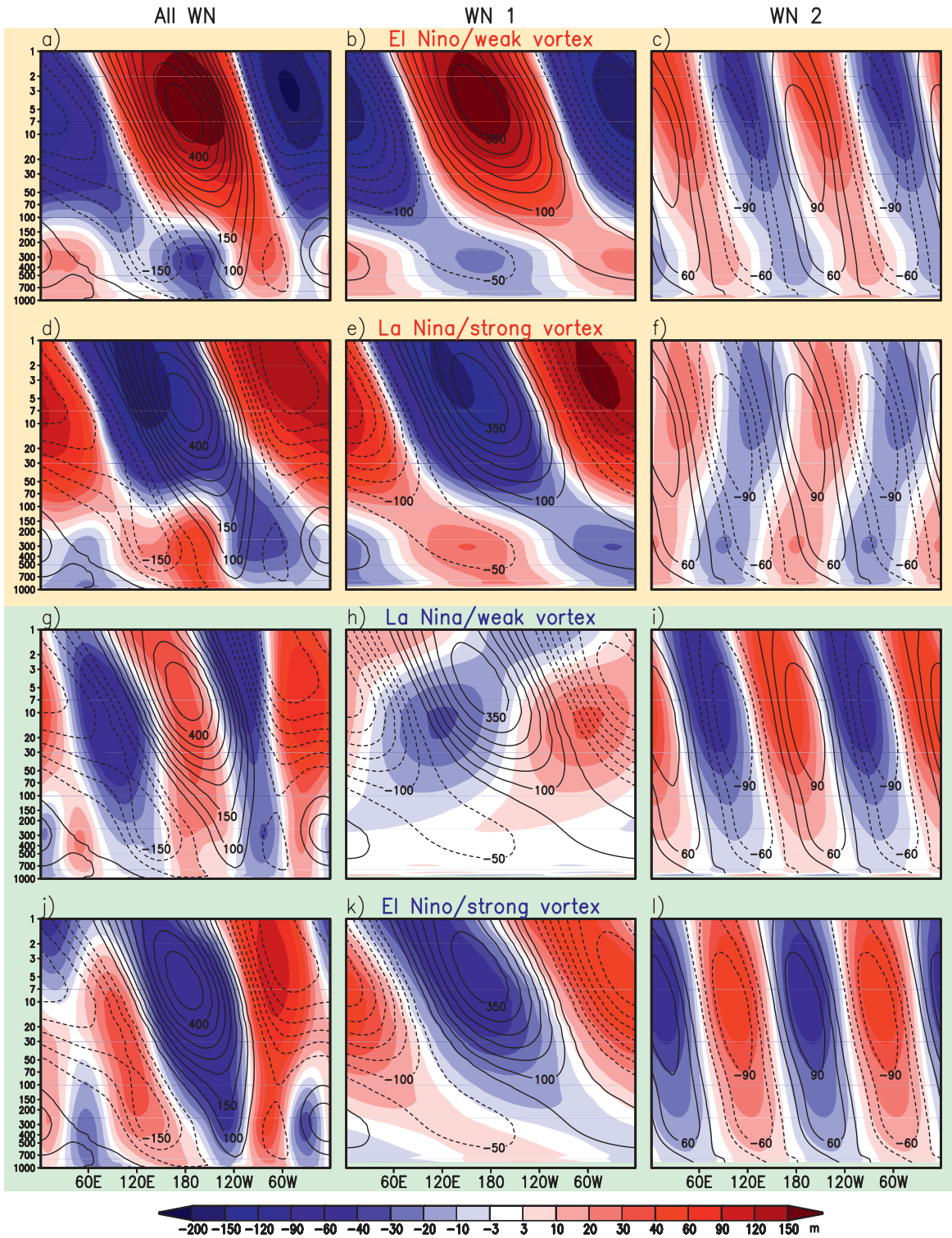


FIG. 8. Panels in the middle and right columns are analogous to those shown in Fig. 5, except for composites over the (top) El Niño/weak vortex, (second row) La Niña/strong vortex, (third row) La Niña/weak vortex, and (bottom) El Niño/strong vortex events. The corresponding results for all zonal wavenumbers are in the left column. Results for the two wave-1 combinations (top half) and two wave-2 combinations (bottom half) are presented with yellow and green backgrounds, respectively.

are 180° out of phase with the background stationary wave (Fig. 8e). On the other hand, wave-2 anomalies tilt eastward with height and are quite weak in amplitude (Fig. 8f), and thus contribute little to the total wave field. These results indicate that the precursory flow pattern in the wave-1 combinations has a strong wave-1 structure in both the troposphere and stratosphere.

In contrast, the anomalous wave fields in the wave-2 combinations (shading in Figs. 8g,j) strongly project onto the wave-2 structure (shading in Figs. 8i,l). For the La Niña/weak vortex events, weak wave-1 anomalies tilts eastward with height, whereas the wave-2 anomalies are approximately in phase with the background stationary wave. For the El Niño/strong vortex events, although both the anomalous wave-1 and -2 structures are 180° out of phase with the climatological pattern, the tropospheric amplitude of the anomalous wave 1 is weak, and is smaller than its wave-2 counterpart in the middle and upper troposphere. Specifically, at 300 hPa, the wave-1 anomalies at 300 hPa are less than 10 m whereas the wave-2 anomalies are as large as 20 m.

The composite results for the four types of combination, as shown in Fig. 8, are in accord with the idealized linear combination as schematically shown at the four corners of Fig. 7. The only exception are the El Niño/strong vortex events, which are considered to be a wave-2 combination but also receive a weak contribution from the wave-1 forcing.

6. Relationship between wave propagation and zonal-mean zonal wind anomalies

a. EP-flux patterns

Rosby wave propagation may be further examined using EP flux cross sections. Figure 9 shows cross sections of the EP fluxes and their divergence averaged over the months of four types of combinations. The EP cross sections are shown for the sum of all zonal wavenumbers (left panels), zonal wave 1 (middle panels), and zonal wave 2 (right panels). All results are based on data at zero time lag relative to selected weak or strong vortex events. The corresponding results based on data at a lag of -1 month (not shown) yield similar EP flux patterns but with weaker amplitude, except for the La Niña/strong vortex events (see Table 2).

For weak vortex events in both phases of ENSO, there is a surplus of upward wave fluxes and strong convergences of the EP flux in the upper stratosphere (Figs. 9a,g). Although the cause of the weak vortex in both cases is the upward propagation of the tropospheric Rossby wave, the contribution of these upward wave flux is mainly from the wave-1 component in El Niño condition (cf. Figs. 9b and 9c), but from the wave-2 component in

the La Niña condition (cf. Figs. 9h and 9i). This is as expected and consistent with previous results, as shown in Figs. 8a–c and 8g–i, that the geopotential height anomaly precursors act to enhance the amplitude of the wave-1 and -2 patterns in the El Niño/weak vortex and La Niña/weak vortex events, respectively.

Conversely, for strong vortex events in both phases of ENSO, the downward EP flux anomaly implies anomalously diminished wave activity (Figs. 9d,j). While the contribution of the downward EP flux is primarily from wave 1 in the La Niña/strong vortex events, the contribution from wave 1 is as important as wave 2 in the El Niño/strong vortex case (Figs. 9k,i). This result is in line with the above mentioned 180° phase difference between the anomalous wave and background climatological pattern for both the wave-1 and -2 components in the latter case (see Figs. 8k,l).

1) VERTICAL PROPAGATION TOWARD THE STRATOSPHERE

The occurrence of strong and weak vortex events has been linked to the upward wave activity entering the stratosphere. It has been shown that time-integrated eddy heat flux is anomalously positive several weeks prior to weak vortex events, and anomalously negative preceding strong vortex events (e.g., Christiansen 2001; Polvani and Waugh 2004).

To measure the upward propagation of planetary waves entering the stratosphere, the anomalous vertical component of the EP flux (F_z) at 100 hPa and averaged over 45° – 75° N is calculated, as in Polvani and Waugh (2004). Table 2 compares the values of F_z for wave-1 and -2 in the four combination types for lags of -1 and 0 month.

For the two wave-1 combination events (i.e., El Niño/weak vortex and La Niña/strong vortex events), the magnitude of the F_z associated with wave-1 is significantly larger than that associated with wave-2 during lags of both -1 and 0 months (see the first four rows in Table 2). In contrast, for the wave-2 combinations, there is evidence of the larger wave-2 component of F_z (see the last four rows in Table 2). However the wave-1 component of F_z is not negligible, except during the lag of 0 month of the La Niña/weak vortex events.

2) MERIDIONAL PROPAGATION IN THE UPPER TROPOSPHERE

Given the importance of the eddy momentum flux in the maintenance of the upper tropospheric zonal wind anomalies, it is of interest to study in more detail the role of the meridional component of the eddy forcing.

The impacts of the stratospheric circulation on the refraction of the vertically propagating waves from the troposphere have been discussed in many previous

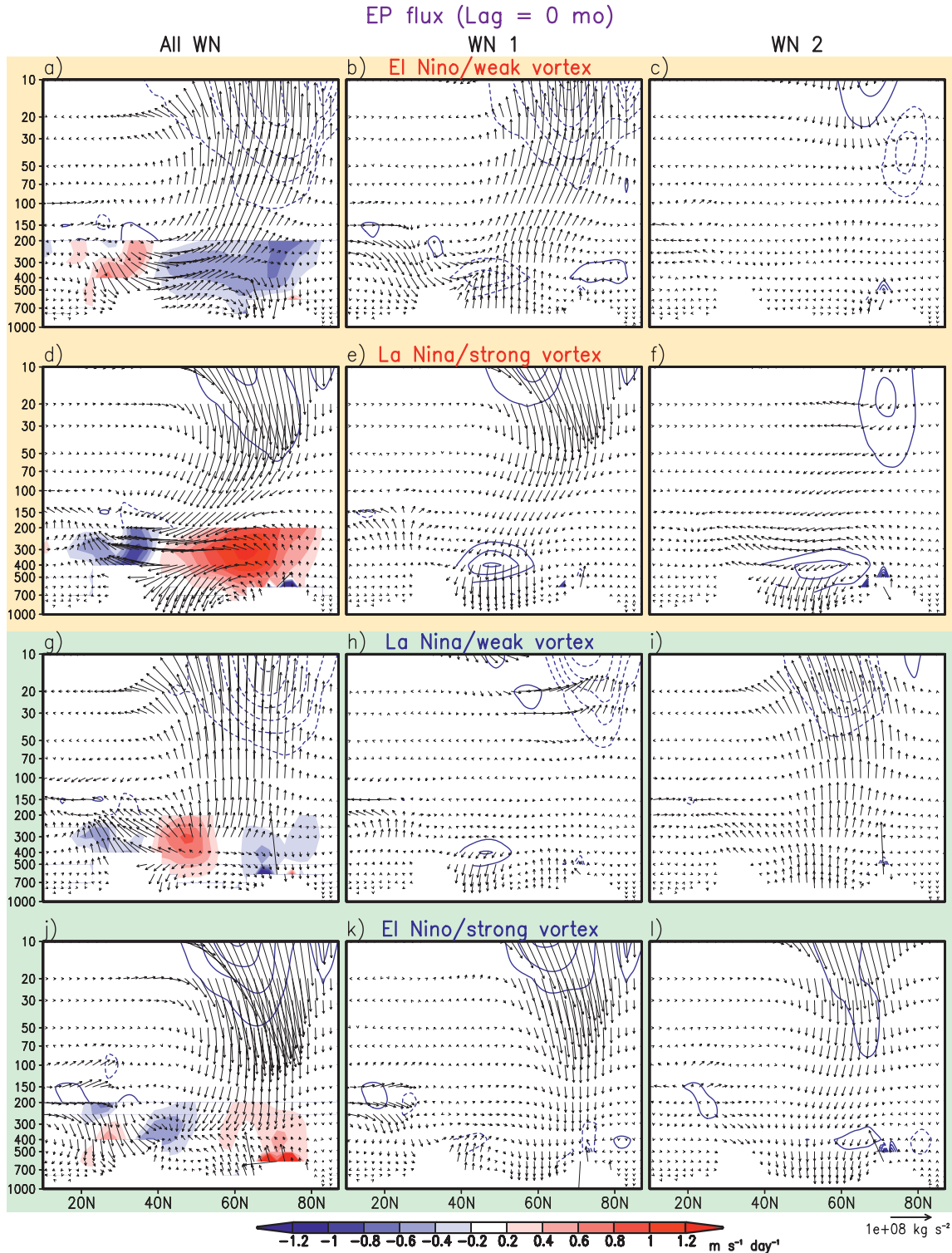


FIG. 9. Composite of latitude–height cross sections of EP flux (divided by the local air density; arrows) and its divergence (D_F ; contours; interval: $0.5 \text{ m s}^{-1} \text{ day}^{-1}$) for (left) all zonal wavenumbers, (middle) zonal wavenumber 1, and (right) zonal wavenumber 2. Shadings below 200 hPa superimposed on the left panels indicate the meridional derivative of F_ϕ (first term in D_F ; see scale at bottom). Composites are averaged over data at a lag of 0 month relative to the (top) El Niño/weak vortex, (second row) La Niña/strong vortex, (third row) La Niña/weak vortex, and (bottom) El Niño/strong vortex events based on the CM3 simulation. The results in this figure are based on the composites over the subsets of weak/strong vortex months in El Niño and La Niña winters (see numbers in parentheses in the second and third rows of Table 1).

TABLE 2. Vertical component of EP fluxes (F_z ; units: 10^3 kg s^{-2}) at 100 hPa averaged over $45^\circ\text{--}75^\circ\text{N}$ for zonal wavenumbers 1 and 2 (second and third column of data entries), during lags of -1 and 0 month of the four types of combination events. Values in bold type indicate anomalies for wavenumber 1 and 2 that are significantly different from each other at the 95% confidence level based on a two-tailed t test. The two-tailed p value for the difference between the wave-1 and wave-2 data in each row is shown in the last column of the same row.

	Lag (month)	$F_z (\times 10^3 \text{ kg s}^{-2})$		p value
		WN 1	WN 2	
El Niño/weak vortex	-1	18.25	0.28	<0.01
	0	23.56	2.52	<0.01
La Niña/strong vortex	-1	-14.32	-7.98	0.03
	0	-12.53	-2.91	<0.01
La Niña/weak vortex	-1	6.65	14.62	0.32
	0	-1.15	21.20	0.02
El Niño/strong vortex	-1	-6.46	-10.20	0.46
	0	-8.19	-12.61	0.42

studies (e.g., Chen and Robinson 1992; Hartmann et al. 2000; Limpasuvan and Hartmann 2000). As shown in Limpasuvan and Hartmann (2000), when the polar vortex is weaker than normal, the increased index of refraction near the subpolar tropopause would enhance the propagation of planetary waves toward the polar region according to Wentzel–Kramers–Brillouin–Jeffries (WKBJ) theory (Andrews et al. 1987). In contrast, stronger than normal polar vortices are accompanied by equatorward refraction of planetary waves in the upper troposphere and lower stratosphere.

The effects of ENSO on meridional wave propagation have been investigated in the diagnostic and modeling study of Seager et al. (2003), who illustrated that strengthening of the subtropical jets during El Niño events could modify the meridional potential vorticity gradient of the zonal flow, and thus the refractive characteristics of the basic state. These changes are conducive to refraction of transient eddies away from the latitudes of the intensified jet. The opposite situation prevails in La Niña events.

We proceed to estimate the typical amplitude of the anomalous meridional component of the EP flux, F_ϕ [see definition in Eq. (1)] at 300 hPa, by compositing over different types of ENSO and polar vortex events separately, using the procedure described in section 5. Since we are primarily interested in the behavior of F_ϕ during the month of anomalous polar vortex, composites are computed for the lag of 0 month for weak/strong vortex events. The ENSO composites are constructed for the period of FM(1), when the simulated ENSO events attain maturity. Analyses based on the vertical levels at 250 and 350 hPa, and on the periods of D(0)J(1) and JF(1) for the simulated ENSO events yield similar results.

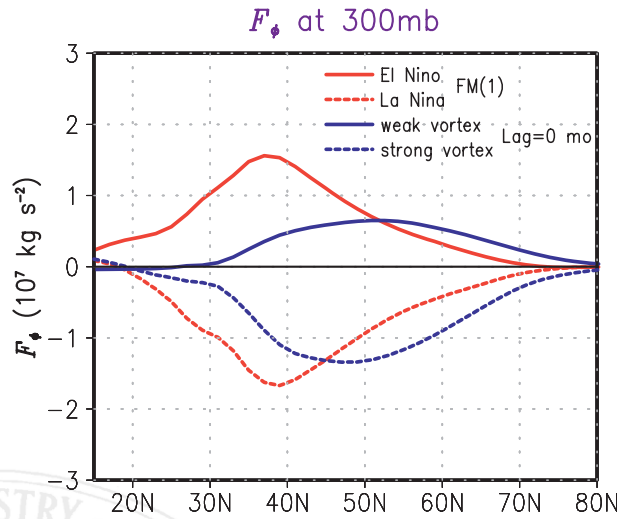


FIG. 10. Composites of the latitudinal profile of anomalous meridional component of EP flux (F_ϕ) at 300 hPa for El Niño (red solid line), La Niña (red dashed line), weak vortex (blue solid line), and strong vortex (blue dashed line) events. The composite is computed using data for the period FM(1) for the ENSO events, and at a lag of 0 month relative to anomalous vortex events.

In agreement with various previous studies cited above, both El Niño and weak vortex events are characterized by positive anomalies of F_ϕ at 300 hPa, indicating poleward refraction of the wave activity in the upper troposphere (see solid lines in Fig. 10). At locations south of 50°N , the magnitude of F_ϕ in El Niño events is larger than in weak vortex events, whereas the reverse situation holds for locations north of 50°N . Analogously, equatorward refraction prevails in La Niña and strong vortex events (see dashed lines Fig. 10).

For the wave-1 combinations (i.e., cases of El Niño/weak vortex or La Niña/strong vortex; see definition in section 5c), the F_ϕ anomaly associated individually with ENSO and polar vortex events have the same polarity and hence reinforce each other. For example, as the composites of F_ϕ in El Niño and weak vortex events are both positive (see two solid lines in Fig. 10), a combination of these two types of events would yield a broad positive anomaly in F_ϕ spanning both middle and high latitudes. This inference is in accordance with the 300-hPa EP flux pattern in Fig. 9a, which shows poleward propagation of F_ϕ at 300 hPa during the El Niño/weak vortex events. Similarly, the combined anomaly of F_ϕ for La Niña and strong vortex cases (see two dashed lines in Fig. 10) is characterized by equatorward propagation in both middle and high latitudes (see also Fig. 9d).

For the wave-2 combination (i.e., cases of El Niño/strong vortex or La Niña/weak vortex), the F_ϕ anomaly associated with ENSO is opposite to that associated with polar vortex events, thus resulting in noticeable

cancellations. For example, when El Niño episodes are combined with strong polar vortex cases, the corresponding changes in F_ϕ (see solid red and dashed blue curves in Fig. 10) are opposite to each other. The net effect (as deduced from the summation of these two curves) is weak poleward F_ϕ flux south of 40°N, and a weak equatorward flux farther north. This inference is consistent with the 300-hPa EP flux pattern in Fig. 9j. Similar cancellations between the effects of La Niña and weak polar vortex on F_ϕ are also evident in Fig. 10.

b. Zonal-mean zonal wind

Previous work has shown the El Niño-related stratospheric signals in the high latitudes (e.g., zonal mean zonal wind at 60°N) propagating downward from the upper stratosphere in early winter to the lower stratosphere and troposphere in late winter (Manzini et al. 2006; Ineson and Scaife 2009). It has been noted in Li and Lau (2012a) that the amplitude of the zonal mean zonal wind at 60°N is reduced by a factor of 10 in the CM2.1 simulation due to its low vertical resolution in the model stratosphere. However, the El Niño-related amplitude of stratospheric signal and its propagating pattern in the CM3 simulation (not shown) exhibits a better agreement with observations and other GCM simulation than the CM2.1 simulation.

The height–time cross section of the stratospheric signals averaged over specific latitudes provides clear and valuable information on the downward propagation of signals at those latitudes, but little information on the meridional structure. For this reason, the height–latitude cross section of the zonal-mean zonal wind during the life cycle of the different combinations of ENSO and polar vortex events are presented in Fig. 11. The composites are based on data at individual lags ranging from -1 to $+2$ month relative to the selected events.

1) DOWNWARD PROPAGATION FROM UPPER STRATOSPHERE TO LOWER STRATOSPHERE

For the El Niño/weak vortex combination, the easterly wind anomaly, which peaks in the upper stratosphere at a lag of 0 month (Fig. 11b), results from the anomalous upward propagating waves and the attendant anomalous convergence of the EP flux in the stratosphere. This zonal flow anomaly descends to the middle and lower stratosphere during the lag of $+1$ and $+2$ months (Figs. 11c,d). It is not clear whether the high-latitude easterly anomalies in the troposphere originate from the descending signals in the lower stratosphere or develop locally.

The evolution of the zonal-mean zonal wind during the La Niña/strong vortex events (Figs. 9e–h) is similar to that in the El Niño/weak vortex events, except for reversal in the polarity of the primary signals.

Inspection of Fig. 11 reveals strong similarities between the stratospheric zonal wind developments in the El Niño/weak vortex (first row) and the La Niña/weak vortex (third row) combinations. The stratospheric wind evolution in the La Niña/strong vortex combination (second row) also bears a notable resemblance to that in the El Niño/strong vortex combination (fourth row) for time lags of -1 to $+1$ months. These results illustrate that the strength of the polar vortex plays a dominant role in the downward migration of the upper stratospheric zonal wind signals to the upper troposphere except at the lag of $+2$ month, whereas the phase of ENSO is only of secondary importance. Although responses to ENSO could vary in models with different background climatological waves (Fletcher and Kushner 2011), given the realistic climatological stationary waves in the CM3 simulation (see Fig. 3), conclusions made based on these model results are considered to be reliable.

2) TROPOSPHERIC WIND ANOMALIES

Although the wind structure is similar in the stratosphere for weak vortex events in both phases of ENSO, notable differences are discernible between the El Niño/weak vortex and La Niña/weak vortex combinations in the troposphere (Fig. 11, first and third rows). The weak vortex events in El Niño winters are characterized by out-of-phase fluctuations in the zonal-mean zonal wind field, with extrema located near 20° and 60°N and the nodal line coinciding with the climatological jet position ($\sim 40^\circ\text{N}$). This dipole pattern is evident from a lag of -1 month through a lag of $+2$ months. However, a persistent tripolar pattern is apparent throughout the weak vortex events during La Niña winters, with positive wind anomalies centered near 45°N and negative anomalies in the subpolar and subtropical latitudes. Similar but opposite signed dipolar and tripolar patterns of the tropospheric wind anomalies are shown for the La Niña/strong vortex and El Niño/strong vortex combinations (second and fourth rows), respectively.

Such dipolar (tripolar) pattern of the zonal-mean zonal wind anomalies is in accord with the dipolar (tripolar) structure of meridional derivative of F_ϕ (see shading in Fig. 9; note that positive and negative meridional derivatives of F_ϕ correspond to eddy momentum flux convergence and divergence, respectively). Throughout the troposphere column, westerly wind anomalies are accompanied by anomalous eddy momentum flux convergence in the upper troposphere (red shading in Fig. 9), and easterly wind anomalies are found in the regions of eddy momentum flux divergence (blue shading in Fig. 9) in the upper troposphere.

It should be noted that the zonal-mean zonal flow in the troposphere is relatively weak. Only the composite

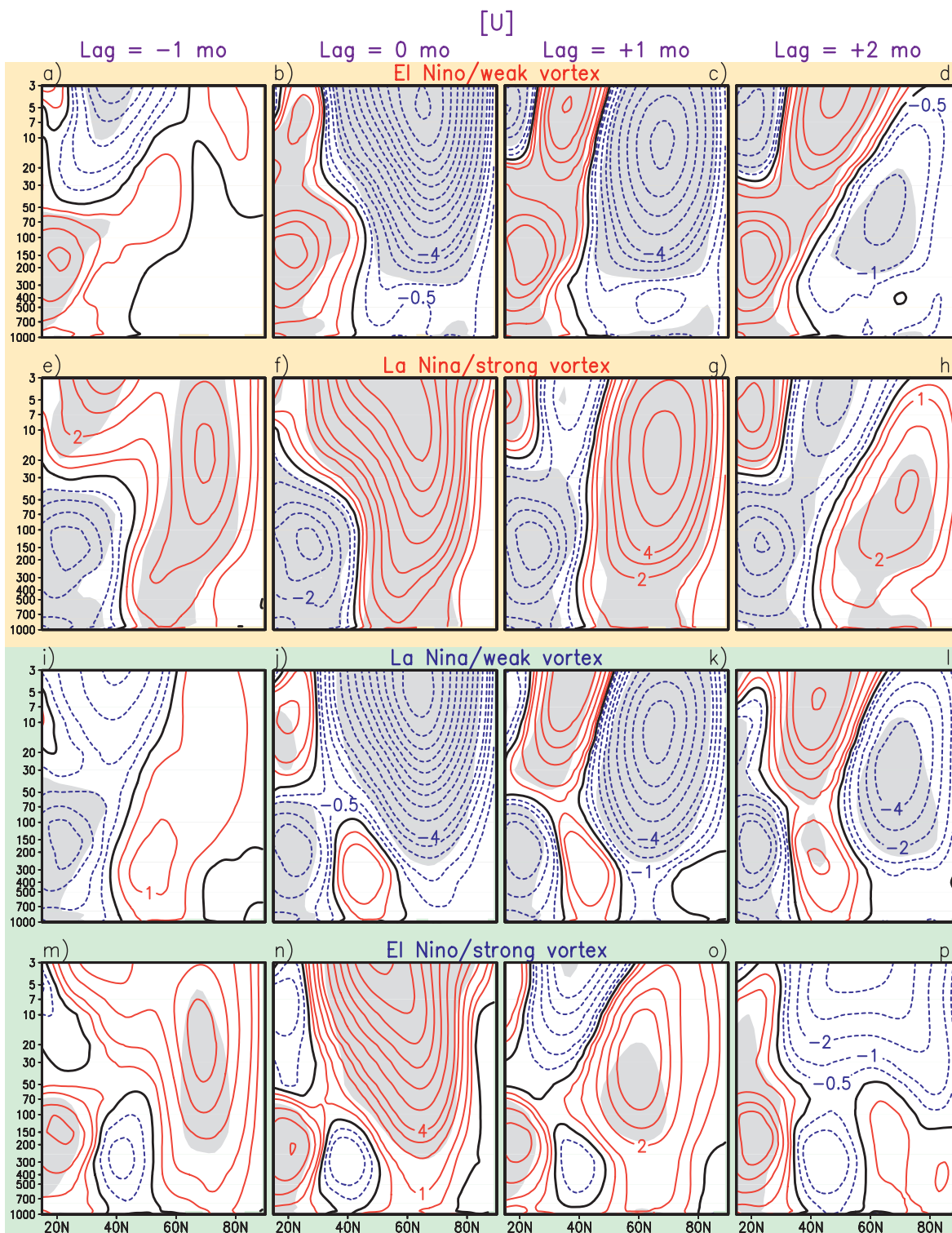


FIG. 11. Composites of latitude–height cross sections of anomalous zonal-mean zonal wind for the (top) El Niño/weak vortex, (second row) La Niña/strong vortex, (third row) La Niña/weak vortex, and (bottom) El Niño/strong vortex events based on CM3 simulation. The composites are computed using data at a lag of (left) -1 , (second column) 0 , (third column) $+1$, and (right) $+2$ months relative to the events. Contours at $0, \pm 0.5, \pm 1, \pm 2, \pm 3, \pm 4, \pm 6, \pm 8 \dots \text{m s}^{-1}$. Gray shading indicates significance at the 95% confidence levels by using a two-tailed Student's t test.

anomalies for the La Niña/strong vortex events are significant at the 95% level using a Student's t test. As indicated in Eq. (4), the acceleration of zonal-mean zonal flow results from both the meridional and vertical convergence of the EP flux, which counteract with each other at tropospheric levels (Thompson et al. 2006; cf. Fig. 9 herein), although the amplitude of the former is larger than the latter. This might partially explain the weak zonal-mean zonal wind response. Nonetheless, the physical consistency of the findings on the upper tropospheric eddy momentum flux convergence, tropospheric zonal-mean zonal wind, and the meridional overturning circulation (see next subsection) lends credibility to the tropospheric signals presented here.

c. Zonal-mean meridional overturning circulation

As discussed in section 5b(2), forcing by the eddy momentum fluxes plays a large role in maintaining the wind anomalies in the upper troposphere. In the lower troposphere, the Coriolis forcing acting on the surface branch of the overturning circulation sustains the near-surface wind anomalies against frictional dissipation (Limpasuvan and Hartmann 2000; Thompson and Wallace 2000). In this subsection, we proceed to show how changes in the upper troposphere are communicated to the surface via the eddy-driven tropospheric overturning circulation.

The anomalous patterns of tropospheric meridional mass streamfunction associated with the four different combinations of ENSO and polar vortex events are presented in Fig. 12. The composites are obtained by averaging over lags of 0 and +1 month relative to the events. These time lags correspond to the period when the tropospheric dipolar/tripolar pattern of the zonal-mean zonal wind anomalies is most distinct in Fig. 11.

For the El Niño/weak vortex events (Fig. 12a), the tropospheric anomalous circulation consists of a two-cell pattern, with a thermally indirect circulation situated in the subtropics, and a weak thermally direct circulation at middle-to-high latitudes. Near the tropopause, anomalous poleward and equatorward flows prevail north and south of 40°N, respectively. This pattern of meridional flow is consistent with that of the meridional derivative of anomalous F_ϕ (see shading in Fig. 9a). The anomalous convergence of the eddy momentum flux south of 40°N (see red shading in Fig. 9a) is primarily balanced by the Coriolis torque acting on the anomalous equatorward flow (Fig. 12a). Conversely, divergence of eddy momentum flux north of 40°N is balanced by a poleward anomalous flow. In the lower troposphere, the poleward (equatorward) flow in the subtropical (high latitude) cell would maintain anomalous surface westerlies (easterlies). Analogous arguments may be invoked to explain

the two-cell pattern for the La Niña/strong vortex combination (Fig. 12b), the polarity of which is opposite to that of the El Niño/weak vortex combination.

The three-cell patterns for the La Niña/weak vortex and El Niño/strong vortex combinations (Figs. 12c,d) are also in accord with the tripolar configuration of the meridional derivative of F_ϕ (see shading in Figs. 9g and 9j), with anomalous poleward (equatorward) flows in the upper troposphere being coincident with eddy momentum flux divergence (convergence). Such three-cell structures would maintain tripolar patterns in the near-surface zonal wind field.

7. Responses of surface annular mode anomalies

It has been shown in previous studies that prominent stratospheric events are followed by tropospheric changes lasting up to 2 months later (Baldwin and Dunkerton 2001; Thompson et al. 2002). To investigate the surface response, the composite mean anomalies in SLP, averaged over the lags of 0, +1, and +2 month relative to the events, are presented in Fig. 13 for the four combination types.

The anomalous SLP field associated with El Niño/weak vortex events (Fig. 13a) is characterized by a positive center of action over the Arctic region, and a negative zonal band at midlatitudes, with prominent features over both the Atlantic and Pacific Oceans. This pattern exhibits a notable zonal symmetry and projects on the negative phase of the surface NAM (e.g., Thompson and Wallace 1998, 2000). The SLP pattern in the region extending from central North America to Europe resembles the negative NAO. The anomalous surface easterly flows near 50°–60°N, as can be inferred from the pattern in Fig. 13a, are accompanied by equatorward flow in the lower branch of the high-latitude meridional cell shown in Fig. 12a. The surface response to La Niña/strong vortex combination (Fig. 13b) captures a zonally symmetric pattern that is similar to the El Niño/weak vortex combination (Fig. 13a), but with opposite polarity.

In contrast, the surface pattern for the La Niña/weak vortex combination (Fig. 13c) is not zonally symmetric. The positive SLP anomaly in the Arctic zone still serves as an indicator of the weakened strength of the polar vortex, as well as its downward influence from the stratosphere. However, the negative midlatitude anomaly over the NA becomes narrower and is displaced northward relative to the pattern in Fig. 13a, and a positive anomaly is apparent in the lower latitudes. As such, the SLP anomaly over NA is characterized by a tripolar pattern in Fig. 13c. This result is consistent with the tripolar pattern of zonal-mean zonal wind in the troposphere (see Figs. 11j–l), and the three-cell structure in Fig. 12c.

F13

F12

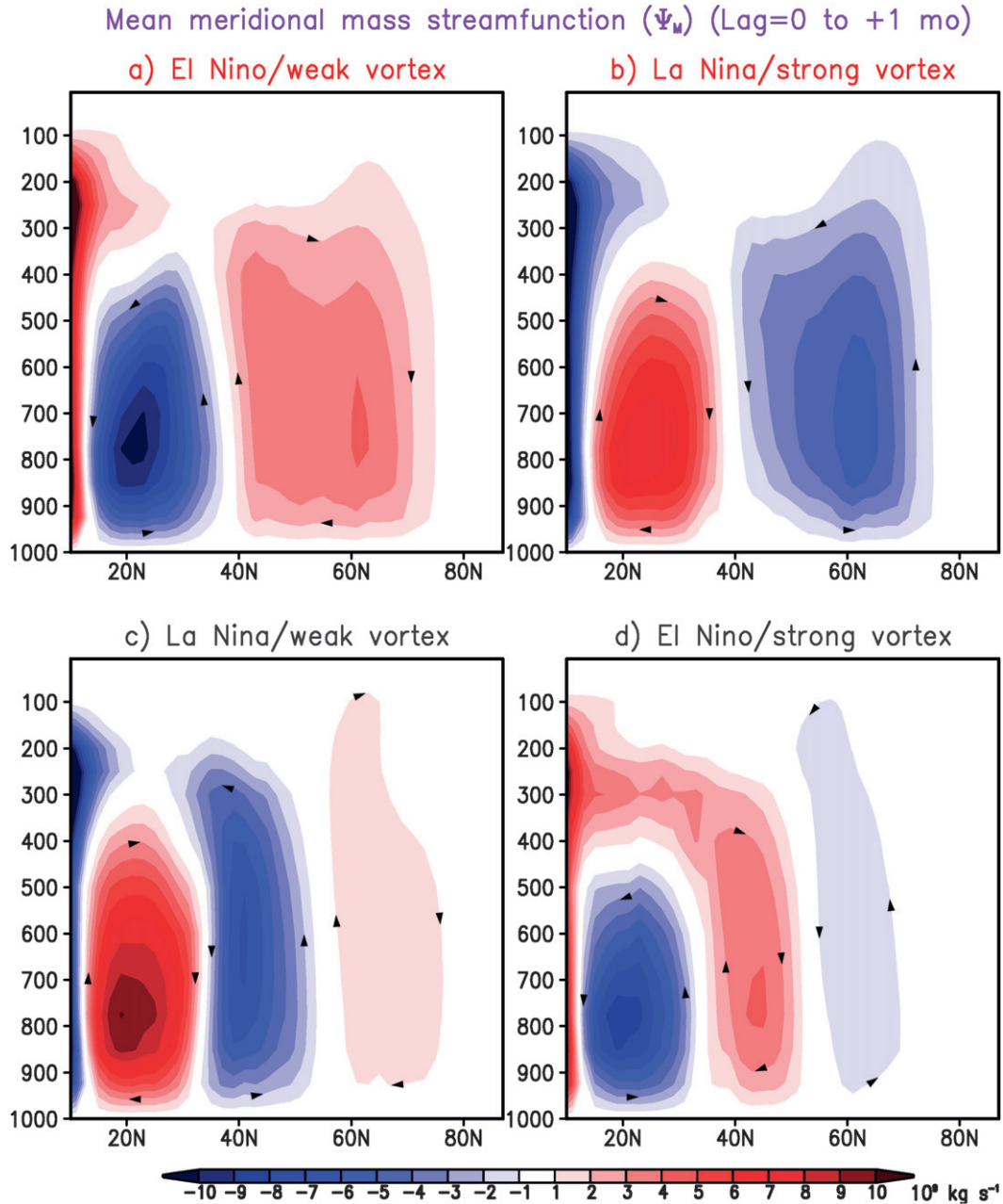


FIG. 12. Composites of anomalous mean meridional mass streamfunction (Ψ_M ; units: 10^9 kg s^{-1}) for (a) El Niño/weak vortex, (b) La Niña/strong vortex, (c) La Niña/weak vortex, and (d) El Niño/strong vortex events. The composites are computed using data averaged over the lags of 0 to +1 month relative to the events. Red and blue shading indicate clockwise and counter clockwise (see arrows) circulation, respectively (see scale bar at bottom).

8. Summary and discussion

The stratospheric pathway in the teleconnection between ENSO and NAO is examined on the basis of a multicentury integration using a coupled GCM with a more realistic upper atmosphere (CM3). As in CM2.1, the ENSO mature phase in the CM3 simulation exhibits

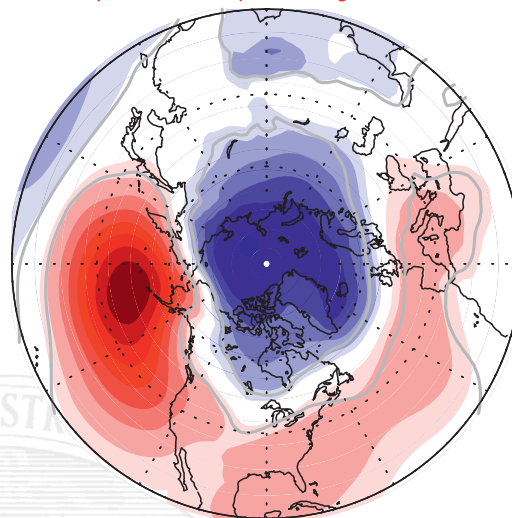
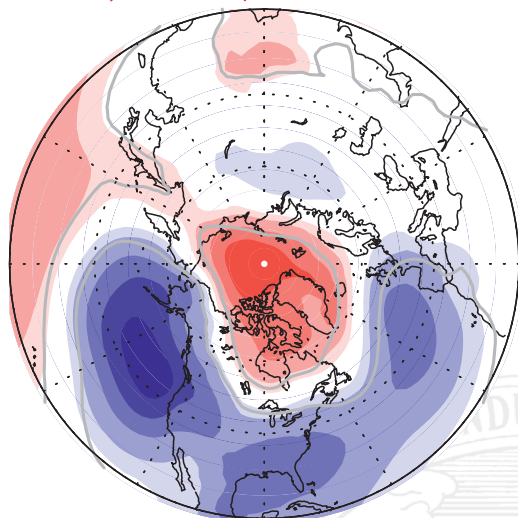
a delay of 1–3 months relative to the observations, but the amplitude of the ENSO event in CM3 is comparable to the observations (Fig. 1).

The ENSO–NAO relationship based on this model simulation is compared to that simulated in CM2.1. It is shown that the enhanced stratospheric resolution in the model does yield a stronger late winter ENSO–NAO

SLP (Lag=0 to +2mo)

a) El Niño/weak vortex

b) La Niña/strong vortex



c) La Niña/weak vortex

d) El Niño/strong vortex

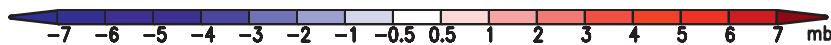
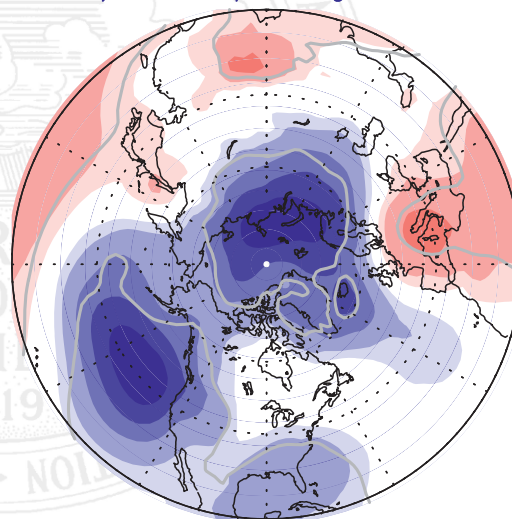
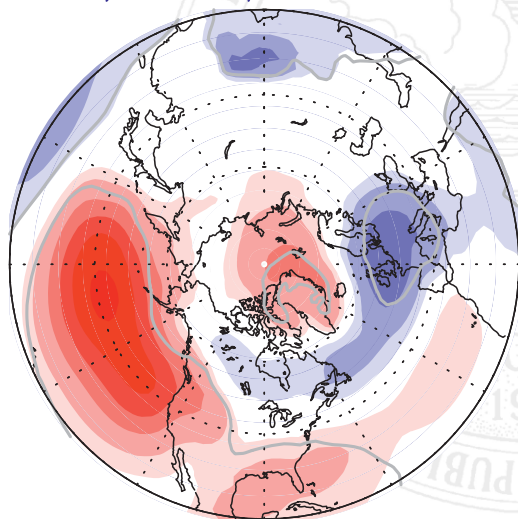


FIG. 13. Horizontal distributions of composites of SLP for the (a) El Niño/weak vortex, (b) La Niña/strong vortex, (c) La Niña/weak vortex, and (d) El Niño/strong vortex based on the CM3 simulation. The composites are computed using data averaged over the lags of 0, +1 and +2 months relative to the events. Gray contours indicate significance at the 95% confidence levels by using a two-tailed Student's *t* test.

relationship, and the amplitude of NAO-like dipolar anomaly in the CM3 simulation is about 20% larger than that in the CM2.1 simulation (Fig. 2). In addition, the CM3 also captures the observed features of both tropospheric and stratospheric climatological stationary waves (Fig. 3).

The model behavior for various combinations between the two opposing phases of ENSO and strong/

weak stratospheric polar vortex events is considered in this study. The key results for weak stratospheric vortex events may be summarized as follows:

- 1) The number of events with weak stratospheric vortex in El Niño winters is notably larger than the counts in La Niña winters (section 4; see Table 1 and Fig. 4).

- 2) The El Niño/weak vortex events are preceded by enhancement of the climatological stationary wave-1 pattern; whereas the La Niña/weak vortex events are preceded by enhancement of stationary wave 2 (section 5; Figs. 7 and 8).
- 3) The upward propagation of wave activity from the troposphere to the stratosphere is mainly due to the wave-1 component in El Niño/weak vortex events, and to the wave-2 component in La Niña/weak vortex events (Fig. 9; Table 2).
- 4) The anomalous easterlies induced by the EP flux convergence north of 60°N propagate downward to the lower stratosphere and upper troposphere during weak vortex events regardless of the ENSO phase (Fig. 11).
- 5) The flow pattern south of 60°N in the upper troposphere is influenced by the meridional wave propagation and the associated pattern of eddy momentum flux convergence at the tropopause level (Fig. 10). The dipolar and tripolar pattern of the eddy momentum flux maintain the dipolar and tripolar pattern of the anomalous zonal-mean zonal wind at the upper troposphere for El Niño/weak vortex and La Niña/weak vortex events, respectively (Fig. 11).
- 6) Changes in the upper troposphere are communicated vertically to the surface via the eddy-driven two-cell and three-cell tropospheric overturning circulation in the El Niño/weak vortex and La Niña/weak vortex events, respectively (Fig. 12). In the 2-month period after the onset of the weakening of the stratospheric vortex, the SLP response over the polar region does appear to be linked to the state of the polar vortex regardless of the phase of ENSO. However, the annular modal pattern is evident only during El Niño winters, and the SLP anomaly resembles the negative NAO in the NA region. On the other hand, the SLP anomaly over NA in La Niña/weak vortex events is characterized by a tripolar pattern (Fig. 13).

Conversely, the number of strong vortex months is notably larger during La Niña events than that during El Niño events. The La Niña/strong vortex events are characterized by the reduced tropospheric wave-1 driving, whereas the El Niño/strong vortex events are associated with the reduction of both wave-1 and wave-2 forcing. The positive phase of the NAO is discernible in the composite SLP pattern for La Niña/strong vortex events (Fig. 13b), but not in the El Niño/strong vortex events (Fig. 13d).

Particular attention is focused on contrasting the behavior in wave-1 combinations (i.e., El Niño/weak vortex and La Niña/strong vortex) against that in wave-2 combinations (i.e., La Niña/weak vortex and El Niño/strong vortex). The number of events in the wave-1

combinations is significantly larger than the counts in the wave-2 combinations (see Table 1). This result indicates that El Niño (La Niña) episodes contributes to weakening (strengthening) of the polar vortex primarily through modulation of the wave-1 component.

Another notable difference between the wave-1 and wave-2 combinations is their effect on the meridional wave refraction (F_ϕ) in the upper troposphere. For the wave-1 combinations, the direction of F_ϕ associated with ENSO is the same as that associated with polar vortex events (Fig. 10). The reinforcement of the individual effects of ENSO and polar vortex changes leads to a dipolar pattern in eddy momentum flux convergence. However, for the wave-2 combinations, the direction of F_ϕ due to ENSO is opposite to that due to polar vortex anomaly. The cancellations between these two separate effects results in a tripolar pattern in eddy momentum flux convergence.

Major midwinter stratospheric sudden warmings (SSWs) are selected using the criteria introduced by Charlton and Polvani (2007). The total number of SSWs based on the 800-yr CM3 simulation is 189 (i.e., 0.24 yr⁻¹). Like many other climate models with a stronger polar vortex (Charlton et al. 2007), the simulated frequency of SSWs is much less than that observed (0.64 yr⁻¹ based on ERA-40). The SSW frequency during the simulated El Niño and La Niña winters are 0.28 yr⁻¹ and 0.23 yr⁻¹, respectively. The almost equal frequency of occurrence of SSWs for El Niño and La Niña winters is consistent with findings in a recent study by Butler and Polvani (2011), who examine the SSW frequency during ENSO winters based on 53 years of reanalysis data. It is plausible that increases of the temperature due to the extreme SSW events on the subseasonal time scale do not necessarily elevate the seasonal-mean temperature field. Thus the statistical relationship between ENSO and SSWs may not be the same as that between the seasonal-mean state of the stratosphere and ENSO.

As mentioned earlier in section 6b(2), the response of the zonal-mean zonal flow in the troposphere is relatively weak and the downward propagating signals are strongly reduced at the tropopause level. Future work is needed to study this problem in more detail with focus on the extreme events, such as SSWs, on time scales of less than a month.

SST anomalies in other ocean basins, particularly the Indian Ocean, may modulate the ENSO influence on NAM. Previous studies have noted opposite-signed zonal mean response to forced SST anomalies over the tropical Pacific Ocean and tropical Indian Ocean (e.g., Branstator and Haupt 1998; Barsugli and Sardeshmukh 2002; Annamalai et al. 2007; Fletcher and Kushner 2011). Specifically, a negative NAM response corresponds to an

imposed warming in the tropical Pacific Ocean, whereas a positive NAM signal is forced by an imposed warming in the tropical Indian Ocean. Recent study by Fletcher and Kushner (2011) has examined the wave responses to warmings imposed in the tropical Indian Ocean, eastern tropical Pacific Ocean, and both. They have found a strong in-phase relationship between wave-1 response and background stationary wave-1 when warming is imposed over the eastern tropical Pacific Ocean and both tropical Indian and eastern Pacific Ocean, whereas an out-of-phase relationship for both wave-1 and -2 is produced for imposed warming in the tropical Indian Ocean. It would be worthwhile to explore the relative importance of warming/cooling over the two ocean basins to the formation of wave-1 and -2 types of combination between ENSO and polar vortex events.

Acknowledgments. We thank Isaac Held, Dave Thompson, Dennis Hartmann, and Chaim Garfinkel for helpful comments and discussions during the preparation of this manuscript. We would also like to thank the three anonymous referees for their thorough reviews and insightful comments, which have led to considerable improvements in this work. This report was prepared by YL under Award NA08OAR4320752 from the National Oceanic and Atmospheric Administration, U.S. Department of Commerce.

REFERENCES

- Ambaum, M. H. P., and B. J. Hoskins, 2002: The NAO troposphere–stratosphere connection. *J. Climate*, **15**, 1969–1978.
- Andrews, D. G., J. R. Holton, and C. B. Leovy, 1987: *Middle Atmosphere Dynamics*. Academic Press, 489 pp.
- Annamalai, H., H. Okajima, and M. Watanabe, 2007: Possible impact of the Indian Ocean SST on the Northern Hemisphere circulation during El Niño. *J. Climate*, **20**, 3164–3189.
- Baldwin, M. P., and D. O’Sullivan, 1995: Stratospheric effects of ENSO-related tropospheric circulation anomalies. *J. Climate*, **8**, 649–667.
- , and T. J. Dunkerton, 2001: Stratospheric harbingers of anomalous weather regimes. *Science*, **294**, 581–584.
- , and D. W. J. Thompson, 2009: A critical comparison of stratosphere–troposphere coupling indices. *Quart. J. Roy. Meteor. Soc.*, **135**, 1661–1672.
- Barsugli, J. J., and P. D. Sardeshmukh, 2002: Global atmospheric sensitivity to tropical SST anomalies throughout the Indo-Pacific basin. *J. Climate*, **15**, 3427–3442.
- Bell, C. J., L. J. Gray, A. J. Charlton-Perez, M. M. Joshi, and A. A. Scaife, 2009: Stratospheric communication of El Niño teleconnections to European winter. *J. Climate*, **22**, 4083–4096.
- Bjerknes, J., 1969: Atmospheric teleconnections from the equatorial Pacific. *Mon. Wea. Rev.*, **97**, 163–172.
- Black, R. X., 2002: Stratospheric forcing of surface climate in the Arctic Oscillation. *J. Climate*, **15**, 268–277.
- Branstator, G., and S. E. Haupt, 1998: An empirical model of barotropic atmospheric dynamics and its response to tropical forcing. *J. Climate*, **11**, 2645–2667.
- Branston, A., and R. E. Livezey, 1987: Classification, seasonality and persistence of low-frequency circulation patterns. *Mon. Wea. Rev.*, **115**, 1083–1126.
- Brönnimann, S., 2007: Impact of El Niño–Southern Oscillation on European climate. *Rev. Geophys.*, **45**, RG3003, doi:10.1029/2006RG000199.
- , J. Luterbacher, J. Staehelin, T. M. Svendby, G. Hansen, and T. Svencø, 2004: Extreme climate of the global troposphere and stratosphere in 1940–42 related to El Niño. *Nature*, **431**, 971–974.
- Butler, A. H., and L. M. Polvani, 2011: El Niño, La Niña, and stratospheric sudden warmings: A re-evaluation in light of the observational record. *Geophys. Res. Lett.*, **38**, L13807, doi:10.1029/2011GL048084.
- Cagnazzo, C., and E. Manzini, 2009: Impact of the stratosphere on the winter tropospheric teleconnections between ENSO and the North Atlantic and European region. *J. Climate*, **22**, 1223–1238.
- Camp, C. D., and K.-K. Tung, 2007: Stratospheric polar warming by ENSO in winter: A statistical study. *Geophys. Res. Lett.*, **34**, L04809, doi:10.1029/2006GL028521.
- Charlton, A. J., and L. M. Polvani, 2007: A new look at stratospheric sudden warmings. Part I: Climatology and modeling benchmarks. *J. Climate*, **20**, 449–469.
- , and Coauthors, 2007: A new look at stratospheric sudden warmings. Part II: Evaluation of numerical model simulations. *J. Climate*, **20**, 470–488.
- Charney, J. G., and P. G. Drazin, 1961: Propagation of planetary-scale disturbances from the lower into the upper atmosphere. *J. Geophys. Res.*, **66**, 83–109.
- Chen, G., and I. M. Held, 2007: Phase speed spectra and the recent poleward shift of Southern Hemisphere surface westerlies. *Geophys. Res. Lett.*, **34**, L21805, doi:10.1029/2007GL031200.
- Chen, P., and W. A. Robinson, 1992: Propagation of planetary waves between the troposphere and stratosphere. *J. Atmos. Sci.*, **49**, 2533–2545.
- Christiansen, B., 2001: Downward propagation of zonal mean zonal wind anomalies from the stratosphere to the troposphere: Model and reanalysis. *J. Geophys. Res.*, **106**, 27 307–27 322.
- Donner, L. J., and Coauthors, 2011: The dynamical core, physical parameterizations, and basic simulation characteristics of the atmospheric component AM3 of the GFDL Global Coupled Model CM3. *J. Climate*, **24**, 3484–3519.
- Dunkerton, T., C.-P. F. Hsu, and M. E. McIntyre, 1981: Some Eulerian and Lagrangian diagnostics for a model stratospheric warming. *J. Atmos. Sci.*, **38**, 819–843.
- Edmon, H. J., B. J. Hoskins, and M. E. McIntyre, 1980: Eliassen–Palm cross sections for the troposphere. *J. Atmos. Sci.*, **37**, 2600–2616.
- Fletcher, C. G., and P. J. Kushner, 2011: The role of linear interference in the annular mode response to tropical SST forcing. *J. Climate*, **24**, 778–794.
- García-Herrera, R., N. Calvo, R. R. Garcia, and M. A. Giorgetta, 2006: Propagation of ENSO temperature signals into the middle atmosphere. *J. Geophys. Res.*, **111**, D06101, doi:10.1029/2005JD006061.
- Garfinkel, C. I., and D. L. Hartmann, 2008a: Different ENSO teleconnections and their effects on the stratospheric polar vortex. *J. Geophys. Res.*, **113**, D18114, doi:10.1029/2008JD009920.
- , and —, 2008b: Effects of the El Niño–Southern Oscillation and the quasi-biennial oscillation on polar temperatures in the stratosphere. *J. Geophys. Res.*, **112**, D19112, doi:10.1029/2007JD008481.

- , —, and F. Sassi, 2010: Tropospheric precursors of anomalous Northern Hemisphere stratospheric polar vortices. *J. Climate*, **23**, 3282–3299.
- Giorgetta, M. A., E. Manzini, R. Roeckner, M. Esch, and L. Bengtsson, 2006: Climatology and forcing of the quasi-biennial oscillation in the MAECHAM5 model. *J. Climate*, **19**, 3882–3901.
- Gnanadesikan, A., and Coauthors, 2006: GFDL's CM2 global coupled climate models, Part II: The baseline ocean simulation. *J. Climate*, **19**, 675–697.
- Griffies, S. M., 2009: Elements of MOM4p1. GFDL Ocean Group Tech. Rep. 6, NOAA/Geophysical Fluid Dynamics Laboratory, 443 pp. [Available online at <http://data.gfdl.noaa.gov/~arl/pubrel/r/mom4p1/src/mom4p1/doc/guide4p1.pdf>.]
- , M. J. Harrison, R. C. Pacanowski, and A. Rosati, 2004: A technical guide to MOM4. GFDL Ocean Group Tech. Rep. 5, NOAA/Geophysical Fluid Dynamics Laboratory, 342 pp.
- , and Coauthors, 2005: Formulation of an ocean model for global climate simulations. *Ocean Sci.*, **1**, 45–79.
- Hamilton, K., 1993: An examination of observed Southern Oscillation effects in the Northern Hemisphere stratosphere. *J. Atmos. Sci.*, **50**, 3468–3473.
- Hartley, D. E., J. T. Villarín, R. X. Black, and C. A. Davis, 1998: A new perspective on the dynamical link between the stratosphere and troposphere. *Nature*, **391**, 471–474.
- Hartmann, D. L., J. M. Wallace, V. Limpasuvan, D. W. J. Thompson, and J. R. Holton, 2000: Can ozone depletion and global warming interact to produce rapid climate change? *Proc. Natl. Acad. Sci. USA*, **97**, 1412–1417.
- Haynes, P. H., M. E. McIntyre, T. G. Shepherd, C. J. Marks, and K. P. Shine, 1991: On the “downward control” of extratropical diabatic circulations by eddy-induced mean zonal forces. *J. Atmos. Sci.*, **48**, 651–678.
- Holton, J. R., and H. C. Tan, 1980: The influence of the equatorial quasi-biennial oscillation on the global circulation at 50 mb. *J. Atmos. Sci.*, **37**, 2200–2208.
- , and —, 1982: The quasi-biennial oscillation in the Northern Hemisphere lower stratosphere. *J. Meteor. Soc. Japan*, **60**, 140–148.
- Horel, J. D., and J. M. Wallace, 1981: Planetary-scale atmospheric phenomena associated with the Southern Oscillation. *Mon. Wea. Rev.*, **109**, 813–829.
- Hurrell, J. W., 1995: Transient eddy forcing of the rotational flow during northern winter. *J. Atmos. Sci.*, **52**, 2286–2301.
- , and H. van Loon, 1997: Decadal variations in climate associated with the North Atlantic Oscillation. *Climate Change*, **36**, 301–326.
- Ineson, S., and A. A. Scaife, 2009: The role of the stratosphere in the European climate response to El Niño. *Nat. Geosci.*, **2**, 32–36, doi:10.1038/ngeo381.
- Kolstad, E. W., and A. J. Charlton-Perez, 2011: Observed and simulated precursors of stratospheric polar vortex anomalies in the Northern Hemisphere. *Climate Dyn.*, **37**, 1443–1456, doi:10.1007/s00382-010-0919-7.
- , T. Breiteig, and A. A. Scaife, 2010: The association between stratospheric weak polar vortex events and cold air outbreaks in the Northern Hemisphere. *Quart. J. Roy. Meteor. Soc.*, **136**, 886–893, doi:10.1002/qj.620.
- Kushner, P. J., and L. M. Polvani, 2004: Stratosphere–troposphere coupling in a relatively simple AGCM: The role of eddies. *J. Climate*, **17**, 629–639.
- Li, Y., and N.-C. Lau, 2012a: Impact of ENSO on the atmospheric variability over the North Atlantic in late winter – Role of transient eddies. *J. Climate*, **25**, 320–342.
- , and —, 2012b: Contributions of downstream eddy development to the teleconnection between ENSO and atmospheric circulation over the North Atlantic. *J. Climate*, **25**, 4993–5010.
- Limpasuvan, V., and D. L. Hartmann, 2000: Wave-maintained annular modes of climate variability. *J. Climate*, **13**, 4414–4429.
- , —, D. W. J. Thompson, K. Jeev, and Y. L. Yung, 2005: Stratosphere–troposphere evolution during polar vortex intensification. *J. Geophys. Res.*, **110**, D24101, doi:10.1029/2005JD006302.
- Lin, S.-J., 2004: A “vertically Lagrangian” finite-volume dynamical core for global models. *Mon. Wea. Rev.*, **132**, 2293–2307.
- Manzini, E., M. A. Giorgetta, M. Esch, L. Kornblueh, and E. Roeckner, 2006: The influence of sea surface temperatures on the northern winter stratosphere: Ensemble simulations with the MAECHAM5 model. *J. Climate*, **19**, 3863–3881.
- Perlwitz, J., and N. Harnik, 2003: Observational evidence of a stratospheric influence on the troposphere by planetary wave reflection. *J. Climate*, **16**, 3011–3026.
- , and —, 2004: Downward coupling between the stratosphere and troposphere: The relative roles of wave and zonal mean processes. *J. Climate*, **17**, 4902–4909.
- Polvani, L. M., and D. W. Waugh, 2004: Upward wave activity flux as precursor to extreme stratospheric events and subsequent anomalous weather regimes. *J. Climate*, **17**, 3548–3554.
- Putman, W. M., and S.-J. Lin, 2007: Finite-volume transport on various cubed-sphere grids. *J. Comput. Phys.*, **227**, 55–78.
- Sassi, F., K. Kinnison, B. A. Boville, R. R. Garcia, and R. Roble, 2004: Effect of El Niño–Southern Oscillation on the dynamical, thermal, and chemical structure of the middle atmosphere. *J. Geophys. Res.*, **109**, D17108, doi:10.1029/2003JD004434.
- Seager, R., N. Harnik, Y. Kushnir, W. Robinson, and J. Miller, 2003: Mechanisms of hemispherically symmetric climate variability. *J. Climate*, **16**, 2960–2978.
- Shindell, D. T., G. A. Schmidt, R. L. Miller, and D. Rind, 2001: Northern Hemisphere winter climate response to greenhouse gas, ozone, solar, and volcanic forcing. *J. Geophys. Res.*, **106**, 7193–7210.
- Smith, T. M., R. W. Reynolds, T. C. Peterson, and J. Lawrimore, 2008: Improvements to NOAA's historical merged land–ocean surface temperature analysis (1880–2006). *J. Climate*, **21**, 2283–2296.
- Song, Y., and W. A. Robinson, 2004: Dynamical mechanisms for stratospheric influences on the troposphere. *J. Atmos. Sci.*, **61**, 1711–1725.
- Stern, W. F., and R. T. Pierrehumbert, 1988: The impact of an orographic gravity wave drag parameterization on extended range predictions with a GCM. Preprints, *Eighth Conf. on Numerical Weather Prediction*, Baltimore, MD, Amer. Meteor. Soc., 745–750.
- Taguchi, M., and D. L. Hartmann, 2006: Increased occurrence of stratospheric sudden warmings during El Niño as simulated by WACCM. *J. Climate*, **19**, 324–332.
- Thompson, D. W. J., and J. M. Wallace, 1998: The Arctic oscillation signature in the wintertime geopotential height and temperature fields. *Geophys. Res. Lett.*, **25**, 1297–1300.

- , and —, 2000: Annular modes in the extratropical circulation. Part I: Month-to-month variability. *J. Climate*, **13**, 1000–1016.
- , M. P. Baldwin, and J. M. Wallace, 2002: Stratospheric connection to Northern Hemisphere wintertime weather: Implications for predictions. *J. Climate*, **15**, 1421–1428.
- , J. C. Furtado, and T. G. Shepherd, 2006: On the tropospheric response to anomalous stratospheric wave drag and radiative heating. *J. Atmos. Sci.*, **63**, 2616–2629.
- Trenberth, K. E., G. W. Branstator, D. Karoly, A. Kumar, N.-C. Lau, and C. Ropelewski, 1998: Progress during TOGA in understanding and modeling global teleconnections associated with tropical sea surface temperatures. *J. Geophys. Res.*, **103**, 14 291–14 324.
- Uppala, S. M., and Coauthors, 2005: The ERA-40 Re-Analysis. *Quart. J. Roy. Meteor. Soc.*, **131**, 2961–3012.
- Vallis, G. K., 2006: *Atmospheric and Oceanic Fluid Dynamics: Fundamentals and Large-Scale Circulation*. Cambridge University Press, 561 pp.
- van Loon, H., and K. Labitzke, 1987: The Southern Oscillation. Part V: The anomalies in the lower stratosphere of the Northern Hemisphere in winter and a comparison with the quasi-biennial oscillation. *Mon. Wea. Rev.*, **115**, 357–369.
- Xue, Y., T. M. Smith, and R. W. Reynolds, 2003: Interdecadal changes of 30-yr SST normals during 1871–2000. *J. Climate*, **16**, 1601–1612.

